

**REAL TIME MEASUREMENT OF MODULATION  
TRANSFER FUNCTION FOR ALIGNMENT OF  
SPECTROMETER**



**A Thesis Submitted in Partial Fulfillment of the Requirements for the  
Degree of Master of Science in Applied Physics  
Suranaree University of Technology  
Academic Year 2018**

เทคนิคการวัดค่ามอดูลชันทรานสเฟอ์ฟังก์ชันแบบเรียลไทม์  
สำหรับการจัดตำแหน่งของตัวตรวจวัดสเปกโตรมิเตอร์



วิทยานิพนธ์นี้เป็นส่วนหนึ่งของการศึกษาตามหลักสูตรปริญญาวิทยาศาสตรมหาบัณฑิต  
สาขาวิชาฟิสิกส์ประยุกต์  
มหาวิทยาลัยเทคโนโลยีสุรนารี  
ปีการศึกษา 2561

**REAL TIME MEASUREMENT OF MODULATION TRANSFER  
FUNCTION FOR ALIGNMENT OF SPECTROMETER**

Suranaree University of Technology has approved this thesis submitted in partial fulfillment of the requirements for a Master's Degree.

Thesis Examining Committee



---

(Assoc. Prof. Dr. Sirichok Jungthawan)

Chairperson



---

(Asst. Prof. Dr. Panomsak Meemon)

Member (Thesis Advisor)



---

(Prof. Dr. Joewono Widjaja)

Member



---

(Dr. Sukanya Tachatraiphop)

Member



---

(Prof. Dr. Santi Maensiri)

Vice Rector for Academic  
and Innovationalization



---

(Assoc. Prof. Dr. Worawat Meevasana)

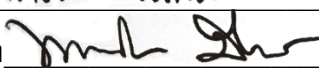
Affairs Dean of Institute of Science

จิราภรณ์ แสนแจ้ : เทคนิคการวัดค่ามอดูเลชันทรานสเฟอ์ฟังก์ชันแบบเรียลไทม์ สำหรับ  
การจัดตำแหน่งของตัวตรวจวัดสเปกโทรมิเตอร์ (REAL TIME MEASUREMENT OF  
MODULATION TRANSFER FUNCTION FOR ALIGNMENT OF SPECTROMETER)  
อาจารย์ที่ปรึกษา : ผู้ช่วยศาสตราจารย์ ดร.พนมศักดิ์ มีมนต์, 61 หน้า

การถ่ายภาพตัดขวางด้วยแสงเลเซอร์/ การออกแบบสเปกโทรมิเตอร์/ ความละเอียดสเปกตรัม/ มอดูเลชัน ทรานสเฟอ์ฟังก์ชัน

ระบบการถ่ายภาพตัดขวางด้วยแสงเลเซอร์ที่เรียกว่า Optical Coherence Tomography หรือ OCT เป็นเทคโนโลยีการถ่ายภาพสามมิติความเร็วสูงแบบไม่ทำลาย ที่ให้ความละเอียดในการถ่ายภาพสูงในระดับ ไมโครมิเตอร์ ซึ่งในปัจจุบัน OCT ได้รับการพิสูจน์และเป็นที่ยอมรับโดยแพทย์ผู้เชี่ยวชาญจากทั่วโลกแล้วว่าเป็นเทคโนโลยีที่สามารถใช้ประโยชน์ในการถ่ายภาพเพื่อใช้ประกอบการวินิจฉัยทางการแพทย์ได้ ซึ่งในระบบการถ่ายภาพตัดขวางด้วยแสงเลเซอร์มีพารามิเตอร์หนึ่งที่สำคัญที่ส่งผลต่อความลึกของการถ่ายภาพของระบบ คือสเปกโทรมิเตอร์ ซึ่งสเปกโทรมิเตอร์มักจะประกอบด้วยเลนส์ เกรตติง และเซ็นเซอร์ โดยที่กำลังแยกเชิงแสงของสเปกโทรมิเตอร์นั้นถูกจำกัดด้วยขนาดพิกเซลของเซ็นเซอร์หรือกำลังแยกของเลนส์โฟกัสของสเปกโทรมิเตอร์ ดังนั้นจึงเป็นสิ่งสำคัญที่จะต้องทำให้สเปกโทรมิเตอร์มีกำลังแยกสูงสุด โดยการลดจุดโฟกัสให้มีขนาดใกล้เคียงหรือเท่ากับขนาดของพิกเซลเซ็นเซอร์ให้มากที่สุด ซึ่งทำได้โดยการจัดวางแนวสเปกโทรมิเตอร์ให้เหมาะสมที่สุด วิทยานิพนธ์นี้นำเสนอเทคนิคเพื่อประเมินประสิทธิภาพด้านกำลังแยกของสเปกโทรมิเตอร์ในระหว่างการจัดตำแหน่งโดยการวัดค่ามอดูเลชันทรานสเฟอ์ฟังก์ชันของระบบสเปกโทรมิเตอร์ควบคู่ไปกับการจัดวางตำแหน่งของอุปกรณ์ ซึ่งทำให้สามารถเพิ่มทั้งความเร็วและความแม่นยำในกระบวนการจัดตำแหน่งสเปกโทรมิเตอร์ ทั้งนี้ กำลังแยกที่เหมาะสมของสเปกโทรมิเตอร์เป็นสิ่งจำเป็นสำหรับการเพิ่มความลึกในการถ่ายภาพของระบบ OCT ซึ่งจะเป็ประโยชน์สำหรับการวินิจฉัยทางการแพทย์ อาทิ การถ่ายภาพผิวหนังและการถ่ายภาพเรตินาในอนาคตต่อไป

สาขาวิชาฟิสิกส์  
ปีการศึกษา 2561

ลายมือชื่อนักศึกษา จิราภรณ์ แสนแจ้  
ลายมือชื่ออาจารย์ที่ปรึกษา 

JIRAPORN SAENJAE : REAL TIME MEASUREMENT OF  
MODULATION TRANSFER FUNCTION FOR ALIGNMENT OF  
SPECTROMETER. THESIS ADVISOR : ASST. PROF. PANOMSAK  
MEEMON, Ph.D. 61 PP.

OPTICAL COHERENCE TOMOGRAPHY/ SPECTROMETER DESIGN/  
SPECTRAL RESOLUTION/ MODULATION TRANSFER FUNCTION

Optical coherence tomography (OCT) is an emerging optical technology that is capable of non-invasive cross-sectional imaging of biological tissues at high-speed, high-resolution, and high sensitivity. OCT has been proven to be a potential tool for medical diagnostics and biomedical researches. One important parameter that governs an imaging depth of spectrometer-based spectral domain OCT (SD-OCT) is the spectral resolution of a spectrometer used in the system. In spectrometer-based SD-OCT that usually composes of a focusing lens, a grating, and a line-array sensor, the effective spectral resolution of the system is either limited by the pixel size of the sensor or the optical resolution of the focusing optics of the spectrometer. Therefore, it is important to maximize the effective spectral resolution of spectrometer to minimize the focus spot close to the diffraction limit spot size and close to the size of the sensor pixel as much as possible, which can only be achieved through optimum alignment of the spectrometer. In this thesis, we have developed a technique to evaluate the spectral resolution of a spectrometer during its alignment process. We have implemented the technique to our custom developed spectrometer to improve its effective spectral resolution and hence the imaging depth of the SD-OCT system, which will be useful

for many medical diagnostics such as skin imaging and retina imaging in the future.



School of Physics

Student's Signature จิรากรณ์ แล่นแจ้

Academic Year 2018

Advisor's Signature 

## ACKNOWLEDGEMENTS

Firstly, I would like to express my sincere gratitude to my advisor Asst. Prof. Dr. Panomsak Meemon for the continuous support of my Master degree and related research, for his patience, motivation, and immense knowledge. His guidance helped me in all the time of research and writing of this thesis. I could not have imagined having a better advisor and mentor for my Master degree.

I would like to thank Mrs. Phenkhae Petchmai and all staffs at the School of Physics, for their kind support. I would also like to thank my colleagues, who have been beside me and helped me in many problems for this thesis: Kunakorn Palawong, Racha pongchalee, Jadsada Saetiew and Yutana Lenaphet. Without their passionate participation, this thesis could not have been successfully conducted.

Finally, I must express my very profound gratitude to my parents for providing me with unfailing support and continuous encouragement throughout my years of study and through the process of researching and writing this thesis. This accomplishment would not have been possible without them. Thank you.

Jiraporn Saenjae

# CONTENTS

	<b>Page</b>
ABSTRACT IN THAI.....	I
ABSTRACT IN ENGLISH.....	II
ACKNOWLEDGEMENTS.....	IV
CONTENTS.....	V
LIST OF TABLES.....	VII
LIST OF FIGURES.....	VIII
<b>CHAPTER</b>	
<b>I INTRODUCTION.....</b>	<b>1</b>
1.1 Background.....	1
1.2 Significance of the study.....	8
1.3 Research objectives.....	9
1.4 Scope and limitations.....	9
<b>II THEORY.....</b>	<b>10</b>
2.1 Optical coherence tomography.....	10
2.2 Spectral domain OCT (SD-OCT).....	13
2.3 Mathematical description of SD-OCT.....	15
2.4 Spectrometer design for SD-OCT.....	22
2.5 Modulation transfer function (MTF).....	25



## CONTENTS (Continued)

	<b>Page</b>
<b>III METHODS.....</b>	<b>27</b>
3.1 MTF measurement technique.....	27
3.2 Spectrum shape adjustment.....	31
3.3 Spectrometer design and implementation.....	32
3.3.1 Lens based spectrometer.....	32
3.3.2 Reflector based spectrometer .....	35
3.4 Spatial frequency in cycles per millimeters.....	37
3.5 Verification of the maximum imaging depth in SD-OCT.....	39
<b>IV RESULTS AND DISCUSSION.....</b>	<b>41</b>
4.1 MTF measurement.....	41
4.1.1 Lens based spectrometer.....	41
4.1.2 Reflector based spectrometer .....	42
4.2 Measurement verification.....	43
4.3 SD-OCT verification.....	47
4.3.1 Lens based spectrometer.....	49
4.3.2 Reflector based spectrometer .....	50
4.4 Comparison of the MTF measurement and the SD-OCT signal drop- off.....	52
4.5 Imaging performance of the system.....	52
<b>V CONCLUSION.....</b>	<b>54</b>
REFERENCES.....	56
CURRICULUM VITAE.....	61

## LIST OF TABLES

Table	Page
1.1 Performance comparison of different designs and configurations of high-speed SD-OCT.....	7
2.1 Examples of recent development of spectrometer SD-OCT.....	21



## LIST OF FIGURES

<b>Figure</b>		<b>Page</b>
1.1	Comparison of OCT resolution and imaging depths to those of alternative techniques; the "pendulum" length represents imaging depth, and the "sphere" size represents resolution.....	2
1.2	Schematic diagram of time domain OCT (TD-OCT) system.....	4
1.3	Schematic diagram of spectral domain OCT (SD-OCT) system.....	4
1.4	The measured sensitivity roll-off over depth of different SD-OCT Configurations.....	7
2.1	Schematic of the low-coherence interferometer.....	11
2.2	Schematic diagram shows axial and transverse resolution of OCT system.....	12
2.3	Typical configurations of swept-source based SD-OCT.....	13
2.4	Typical configurations of spectrometer based SD-OCT.....	14
2.5	Illustration of the depth-resolved reflectivity profile obtained from inverse Fourier transform of the interference spectrum.....	18
2.6	(A) Examples of a broadband spectral signals as a function of $\lambda$ and $\xi$ (B) Reflectivity profile as a function of depth location is a Fourier transform of spectral interference.....	20
2.7	Typical configurations of grating spectrometer setup of (A) lenses-based grating spectrometer and (B) mirrors-based grating spectrometer...	23

## LIST OF FIGURES (Continued)

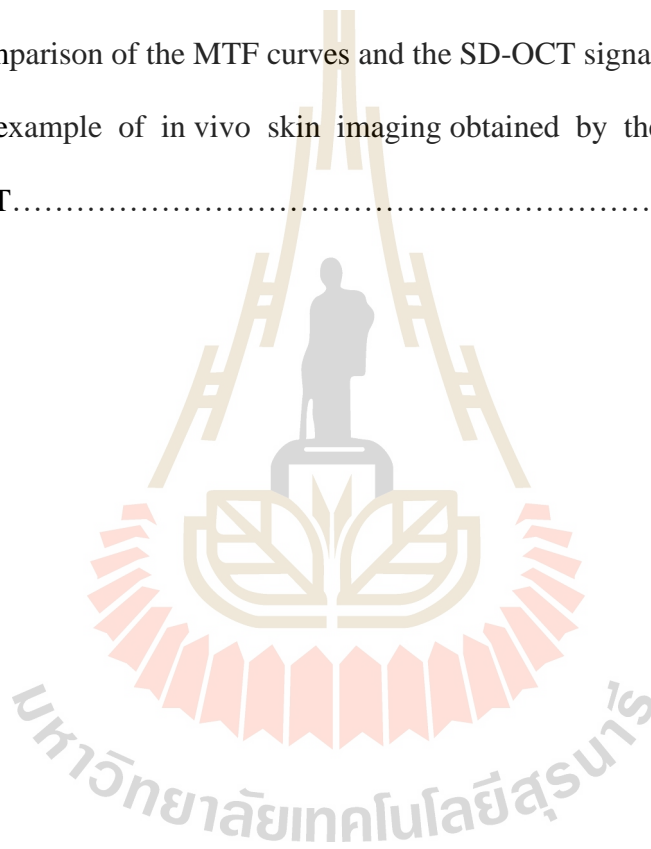
Figure		Page
2.8	Modulation transfer function (MTF) graph.....	26
3.1	The layout of a Michelson interferometer setup for the MTF measurement of the spectrometer.....	28
3.2	The photograph of the LCI setup for the MTF measurement.....	29
3.3	The procedure of MTF calculation.....	30
3.4	The scale factor adjustment can be performed by dividing (A) The modulated spectrum with (B) the non-modulated spectrum of the light source to obtain (C) a uniform modulation amplitude across the sensor region.....	31
3.5	(A-C) The spectrum obtained at different modulation frequencies and the spectrum that can be detected to be divided by data that normalize will get a new shape spectrum as shown in Figure (D-F).....	32
3.6	(A) The power spectrum of the light source. (B) The optical design layout of the spectrometer.....	34
3.7	(A) The power spectrum of the light source. (B) The optical design layout of the spectrometer.....	36
3.8	Schematic limitations of the sensor of both systems.....	38
4.1	MTF plots of different regions of the sensor obtained by the algorithm shown in Figure 3.3.....	41
4.2	MTF plots of different regions of the sensor obtained by the algorithm shown in Figure 3.3.....	42

## LIST OF FIGURES (Continued)

<b>Figure</b>		<b>Page</b>
4.3	MTF plots of different regions of the sensor after adding defocus of the collimator by +0.1 mm.....	43
4.4	MTF plots of different regions of the sensor after defocus of the collimator by -0.1 mm.....	44
4.5	(A) Regions of the sensor of the spectrometer. (B) sensor defocus as simulated in code V software.....	45
4.6	MTF plots of different regions of the sensor after tilting up the off-axis Parabolic Mirror with $45^\circ$ by 2 degrees.....	46
4.7	MTF plots of different regions of the sensor after tilting down the off-axis Parabolic Mirror with $45^\circ$ by 2 degrees.....	47
4.8	Comparison of MTF performance at difference defocus of the collimator in (A) zone 1, (B) zone 2, (C) zone 3, (D) zone 4, and (E) zone 5.....	47
4.9	(A-C) Examples of spectral interference signals as detected by the spectrometer and (D-F) its corresponding depth profiles obtained through the Fourier analysis.....	48
4.10	(A) Plot of the peak amplitude of the SD-OCT signals measured at different depth positions in air. Figure 4.10 (B) Inverse Fourier transform of a fitted curve, representing the shape of the overall effective spectral resolution of the Lenses based Spectrometer.....	50

## LIST OF FIGURES (Continued)

<b>Figure</b>		<b>Page</b>
4.11	(A) Plot of the peak amplitude of the SD-OCT signals measured at different depth positions in air. Figure 4.11 (B) Inverse Fourier transform of a fitted curve, representing the shape of the overall effective spectral resolution of the Reflective Spectrometer.....	51
4.12	Comparison of the MTF curves and the SD-OCT signal drop-off.....	52
4.13	An example of in vivo skin imaging obtained by the developed SD-OCT.....	53



# CHAPTER I

## INTRODUCTION

### 1.1 Background

Optical coherence tomography (OCT) is an imaging technology, which was invented by MIT's researchers lead by James Fujimoto (Huang et al., 1991). OCT has been proven to be an effective and reliable tool for non-invasive characterization. OCT can perform high-speed imaging, which is suitable for real-time imaging and monitoring of biological tissues. It is a tomographic technique that used low temporal coherence property of broadband light source to produce high-resolution depth-sectional images. In addition, OCT uses near-infrared light for non-invasive and non-destructive imaging with less process on sample preparation.

The image formation of OCT is analogous to ultrasound imaging except that OCT utilizes an infrared light beam in oppose with ultrasonic wave in ultrasound imaging for acquiring sample information. The performance of OCT, when compare with other imaging techniques, is in between ultrasound and confocal microscopy as shown in Figure 1

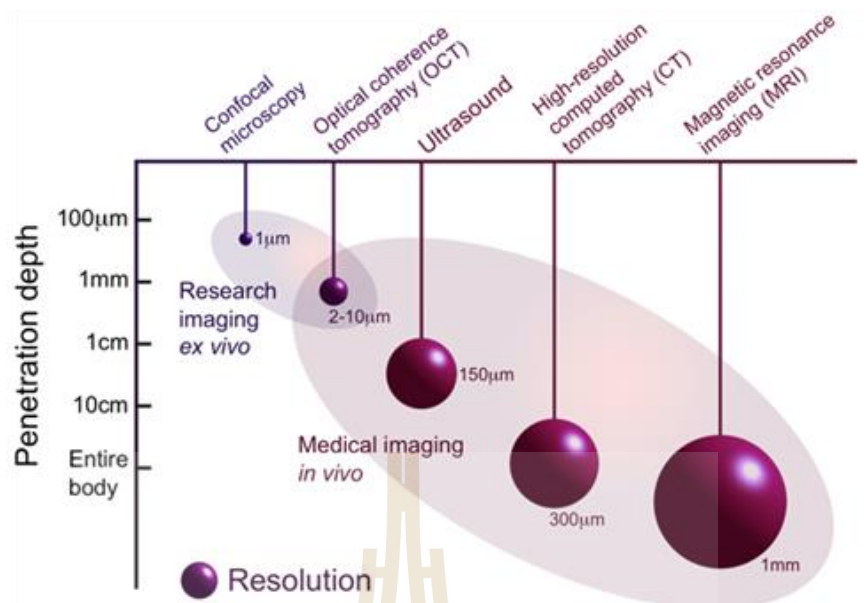


**Figure 1.1** Comparison of OCT resolution and imaging depths to those of alternative techniques; the vertical axis is imaging depth, and the "sphere" size represents resolution.

(photo source: <http://obel.ee.uwa.edu.au/research/fundamentals/introduction-oct/>).

OCT provides high resolution and cross-sectional image by measuring the light intensity reflected from within the micro-structure of biological tissues. To date, OCT have been widely used to characterize cross-section structure of biological tissues and materials because it is low cost, easy to use, and noninvasive nature (Bashkansky et al., 1997). Furthermore, OCT is capable of high resolution 2D and 3D cross-sectional imaging in real time. OCT has been rapidly developed and has been applied in various fields such as medicine, biology, tissue engineering, and material characterization (Götzinger et al., 2005).



Most of OCT system is designed to be used at near-infrared wavelength in range of 800-1300 nm that is known as an optical window of biological tissue, where the light can travel deeper in biological samples with less absorption of blood and water, which are the main components of most biological samples. Therefore, the present development of OCT system commonly uses the wavelength in 800, 1000, and 1300 nm, which are widely available. There are advantages and disadvantages in each wavelength in terms of the imaging resolution and depth penetration in OCT system. The 800 nm wavelength can be used for high-resolution but low-depth penetration, which is capable for a few layers high-resolution under surface imaging. On the other hand, the 1300 nm wavelength is suitable for deeper imaging under sub-layer structure from sample surface but the imaging resolution will be worse than using 800 nm light source at the similar spectral width (Bouma and Tearney, 2002).

The early implementation of OCT performs depth cross-section imaging of a biological sample by scanning the reference mirror as shown in Figure 1.2, so called Time-domain OCT (TD-OCT). As a result, an imaging speed of TD-OCT is limited by the speed of the movable reference mirror. Later, the principle of light interference in frequency domain (Born et al., 1999) is applied in OCT, so called Frequency-domain OCT (FD-OCT) or Spectral-domain OCT (SD-OCT) as shown in Figure 1.3 (Fercher et al., 1995). SD-OCT acquires spectral interference signal from the output of the interferometer. Therefore, SD-OCT has an advantage in sensitivity and acquisition speed because there is no scanning of the reference mirror as compared with TD-OCT (Choma et al., 2003; De Boer et al., 2003; Leitgeb et al., 2003).

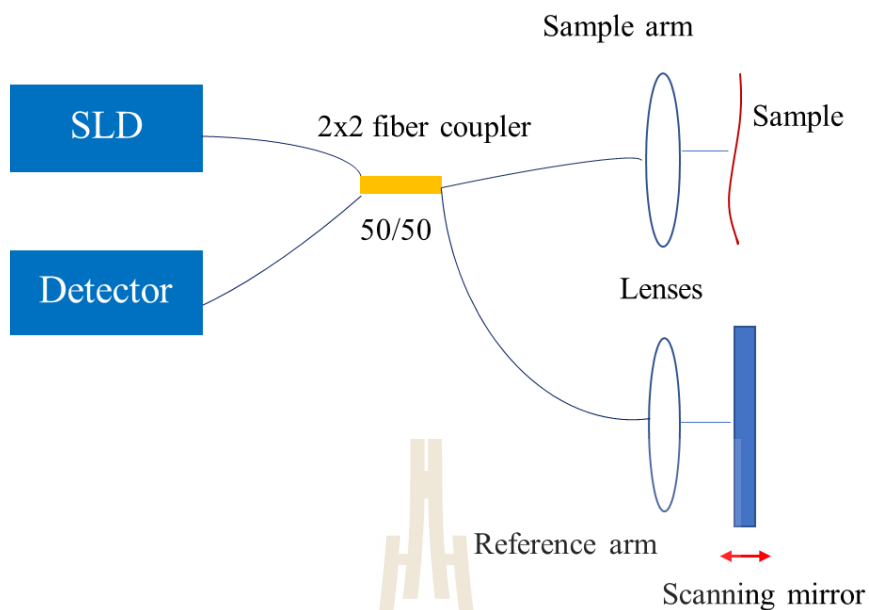


**Figure 1.2** Schematic diagram of time domain OCT (TD-OCT) system.

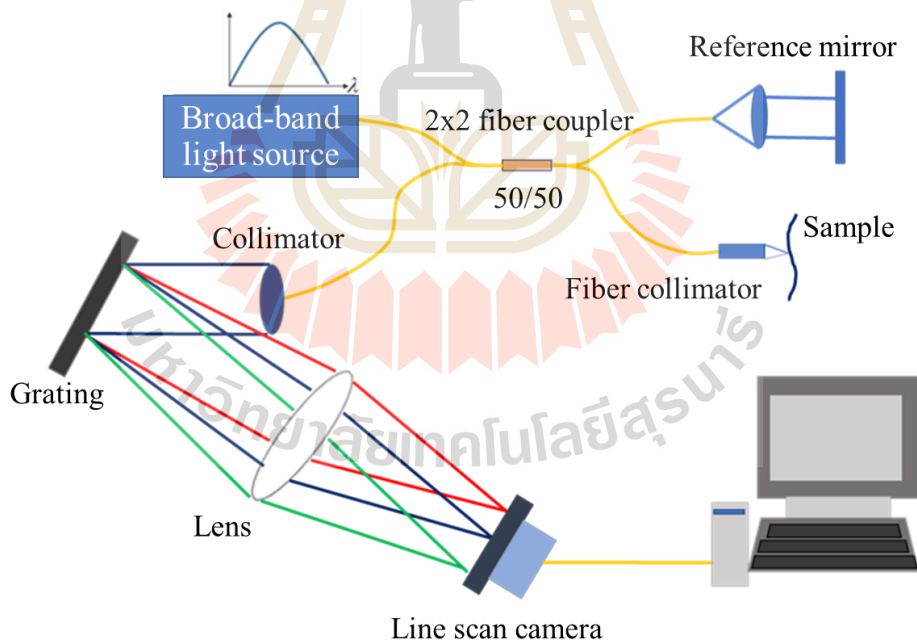


**Figure 1.3** Schematic diagram of spectral domain OCT (SD-OCT) system.

SD-OCT produces a cross-sectional image of a sample by measuring interference spectra between reflecting light from the sample and reference arms. Typically, the

interference spectra are captured by the optical spectrometer and then Fourier transformed to obtain the spatial domain signal related to depth-resolved reflectivity profile of the structures under the surface of the sample. When the beam scanning along to lateral position of the sample is included, the 2D and 3D images can be obtained (Bouma and Tearney, 2002). The use of multi-element array detector and no mechanical scanning of reference beam path of SD-OCT has the advantages of a fast imaging speed over TD-OCT and, thus has been widely employed in 3D OCT imaging. However, SD-OCT has disadvantage of limited imaging depth as compared with TD-OCT that is caused by finite spectral resolution of its detection unit (Fujimoto et al., 2002).

Spectrometer-based SD-OCT usually composes of a focusing lens, a grating, and a line-array sensor. The effective spectral resolution of the system is either limited by the pixel size of the sensor or the optical resolution of the focusing optics of the spectrometer, whichever is smaller. Therefore, it is important to maximum the effective spectral resolution of spectrometer to minimize the focus spot close to the diffraction limit spot size and close to the size of the sensor pixel as much as possible, which can only be achieved through optimum alignment of the spectrometer. Therefore, spectral resolution of a spectrometer used as a detector in each SD-OCT system needs to be measured to verify effective spectral resolution and hence a maximum imaging depth.

In addition, point spread function width is widely used within the OCT literature as an instrument metric (Woolliams et al., 2011, Lee et al., 2009, Woolliams et al., 2010). For spectrometer, the spectral resolution measurement can be performed after each alignment step of the spectrometer by using a tunable narrow line width light source, e.g. stabilized Helium Neon laser, or Argon lamp, or Mercury lamp, as the input

of the spectrometer. This technique usually requires switching of the light source and is not convenient for real time measurement. Moreover, measurement of spectral resolution at different regions of the sensor and/or different wavelengths will require multiple light sources, which prohibits real time measurement.

Additional technique that is especially useful for two dimensional array sensor is by using laser diffraction patterns (Ohlmann and Mego, 1966), which can provide off-axis performance of the spectrometer. However, the technique requires careful alignment of the diffraction patterns on the sensor's area. These techniques are slow measurement processes and need some experience to interpret the results.

Alternatively, the most common method to verify the effective spectral resolution of SD-OCT system is by measuring the trend of sensitivity drop as a function of optical path delay or imaging depth position, so called the sensitivity roll-off measurement. The depth-dependent signal drop is governed by optical resolution limits of the spectrometer. The maximum imaging depth is commonly defined at the depth location where sensitivity is dropped to 10 dB (Bouma and Tearney, 2002; Lee et al., 2009). The trace of the sensitivity roll-off curve is related with the effective spectral resolution by the Fourier transform relation. The sensitivity roll-off measurement is convenient for indirect estimation of the effective spectral resolution and can be used to compare spectral resolution performance of different SD-OCT configurations as shown in Figure 1.4 and Table 1.1. (Potsaid et al., 2008; Lee et al., 2009).

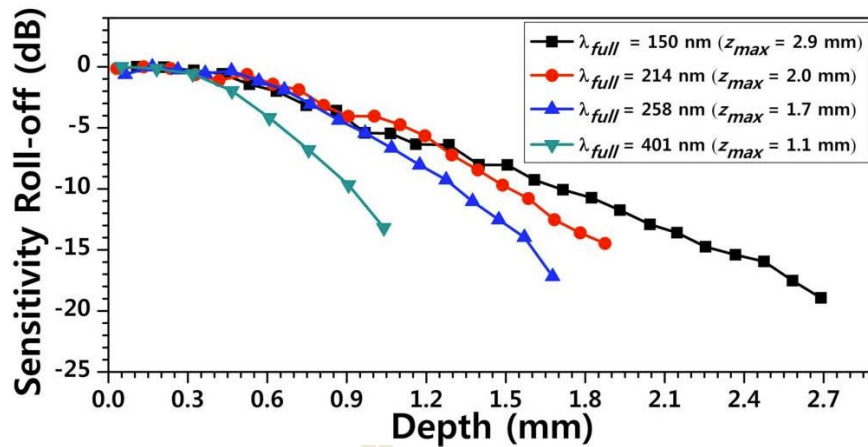


**Figure 1.4** The measured sensitivity roll-off over depth of different SD-OCT configurations (Lee et al., 2009).

**Table 1.1** Performance comparison of different designs and configurations of high-speed SD-OCT (Potsaid et al., 2008).

Design Configuration	A	B	C	D
Camera pixels	4096	2528	800	576
Camera line rate (lines per second)	70,000	106,382	250,000	312,500
Camera line period	14.2 $\mu$ s	9.4 $\mu$ s	4.0 $\mu$ s	3.2 $\mu$ s
Camera exposure time	13.0 $\mu$ s	8.2 $\mu$ s	2.8 $\mu$ s	2.0 $\mu$ s
Light source	2 $\times$ SLD	3 $\times$ SLD	Ti-Sapph	Ti-Sapph
Light source FWHM	144 nm	181 nm	33 nm	27 nm
Spect. collimating lens focal length	70 mm	50 mm	50 mm	50 mm
Spect. focusing lens focal length	160 mm	80 mm	80 mm	80 mm
Calculated depth range in air	4.4 mm	2.1 mm	2.0 mm	2.0 mm
Measured 10 dB roll-off depth	2.36 mm	1.13 mm	1.43 mm	1.26 mm

Table 1.1 shows performance comparison of different configurations of high-speed SD-OCT systems using different ultrahigh-speed CMOS line scan cameras and light sources. Several configurations were designed, implemented, and characterized to illustrate trade-offs between acquisition speed, resolution, imaging range, sensitivity, and sensitivity roll-off performance (Potsaid et al., 2008). From Table 1.1, in all cases, The measured depth ranges are shorter than the theoretical calculated depth ranges. These results imply that, in all cases, the optical spectral resolution is larger than the pixel size of the sensor. The measured and calculated spectral resolution would be approximately the same if the optical resolution of the spectrometer optics were optimized.

## 1.2 Significance of the study

As discussed above, most commonly used spectral resolution measurement techniques for SD-OCT are slow measurement processes and cannot be performed in real time and/or during the alignment process of the spectrometer. Therefore, all these measurement techniques cannot provide information about spectrometer misalignment. A technique that is capable of fast visualizing the effective spectral resolution of a spectrometer during optical alignment process will be extremely useful.

In this work, we have developed a new experimental procedure to evaluate the resolution performance of a spectrometer during an alignment process. The method is based on real time measurement of Modulation Transfer Function (MTF) at different field of view of the spectrometer. The ability to determine MTF performance at different region of the sensor allows for investigation of misaligned component within the spectrometer. The technique can provide both speed and accuracy in spectrometer

alignment process, which can be useful for optimizing the spectrometer's alignment to achieve performance close to the sensor limit resolution of the spectrometer and hence the maximum imaging depth in SD-OCT.

### 1.3 Research objectives

- Developed a new technique to evaluate the resolution performance of a spectrometer during an alignment process by measuring MTF curves at different sensor region in real time.
- Verify the performance of the MTF measurement for alignment of a spectrometer for SD-OCT.

### 1.4 Scope and limitations

- Use a free-space Michelson interferometer to generate modulation of spectrum.
- Develop LabVIEW program for data acquisition and signal processing.
- Design and implement spectrometers at around 800 nm wavelength by use commercially available optical components for verification of the developed MTF measurement technique.
- A CMOS line-array sensor was chosen as the detector.
- The light source was a broadband super luminescent diode 800-880 nm.

## CHAPTER II

### THEORY

#### 2.1 Optical coherence tomography

OCT uses the principle of low-coherence interferometer (LCI), which is typically based-on the Michelson interferometer setup. In the Michelson interferometer, the light source is split into two beams. The first beam is a reference beam, which reflects from the length-adjustable reference mirror to control an optical path delay between the two beams. The second beam is a sample beam, which is focused by the objective lens to the sample. The lens then collects the backscattering light from the sample that corresponds with refractive index variation of the sample structure at different depth. The reflecting light from sample will interfere with the reference light. The optical path difference (OPD) can be adjusted by moving the movable mirror in the reference arm. The cross-sectional image of the sample is created by the amplitude of reflected light at different depths from sample surface (Bouma and Tearney, 2002).

The LCI is a device that produces interference between two beams of light. When two beams of coherence light are combined, their fields rather than their intensities add and produce interference. Figure 2.1 shows a schematic diagram of a simple Michelson interferometer. The source beam is split into two halves. One half is transmitted through the beamsplitter and then back-reflected by a reference mirror. The other half is reflected off the beamsplitter and then back-reflected by an object surface. These two back-reflected beams are recombined by the beamsplitter and then received by a



detector. The interference of a low-coherence light beam only occurs within a short coherence length of a broadband light source. OCT uses this short coherence window to obtain back-scattered light at any specific depth within the sample.

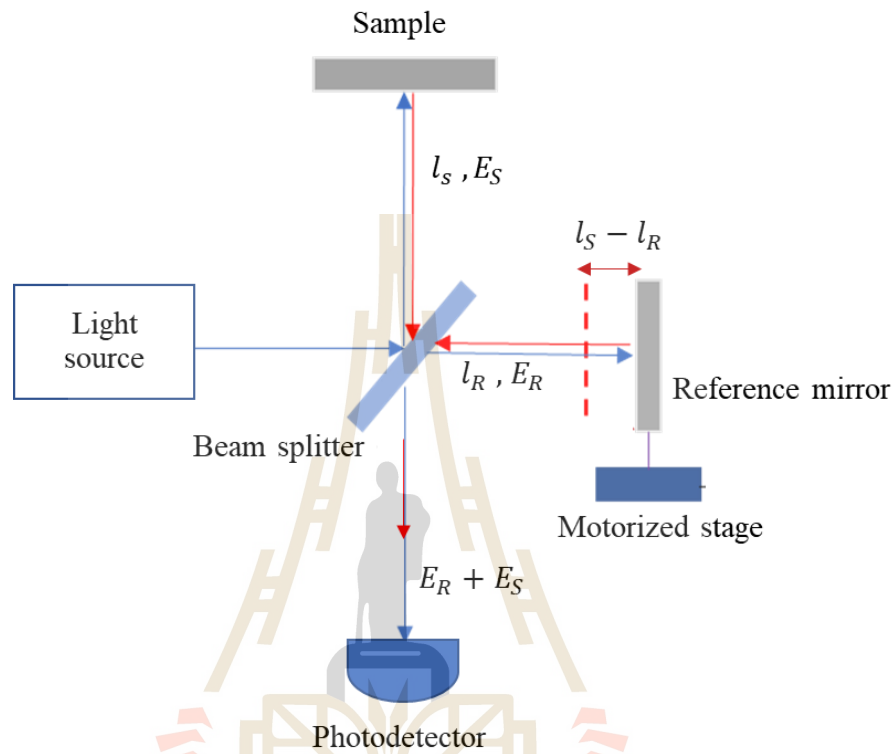


**Figure 2.1** Schematic of the low-coherence interferometer.

OCT uses low-coherence of broadband near-infrared light to detect both the amplitude and depth location of the backscattered light and uses them to construct a cross-sectional image (Bouma and Tearney, 2002). Therefore, the axial resolution in OCT imaging is determined by the coherence length of the light source, Consider the spectrum of the light source distribution as the Gaussian function, the axial resolution  $\Delta Z$  is given as, (Fujimoto et al., 2002).

$$\Delta Z = \frac{2 \ln 2}{\pi} \left( \frac{\lambda^2}{\Delta \lambda} \right), \quad (2.1)$$

where  $\lambda$  is the center wavelength of the source,  $\Delta Z$  is the full-width at half maximum of the autocorrelation function of the power spectrum of the light source, which has bandwidth equal to  $\Delta\lambda$  (Fujimoto et al., 2002).

On the other hand, the transverse resolution of OCT is determined by the focus spot of an optical beam that incidents on the sample. The diffraction limited focus spot size of the conventional focusing lens is inversely proportional to the numerical aperture of the focus beam, which is given as (Fujimoto et al., 2002).

$$\Delta x = \frac{1.22\lambda f}{D}, \quad (2.2)$$

where  $f$  is a focal length and  $D$  is the beam diameter incidence on the objective lens as shown in Figure 2.2. Therefore, high transverse resolution can be obtained by using a large numerical aperture to focus the beam to a small spot size.

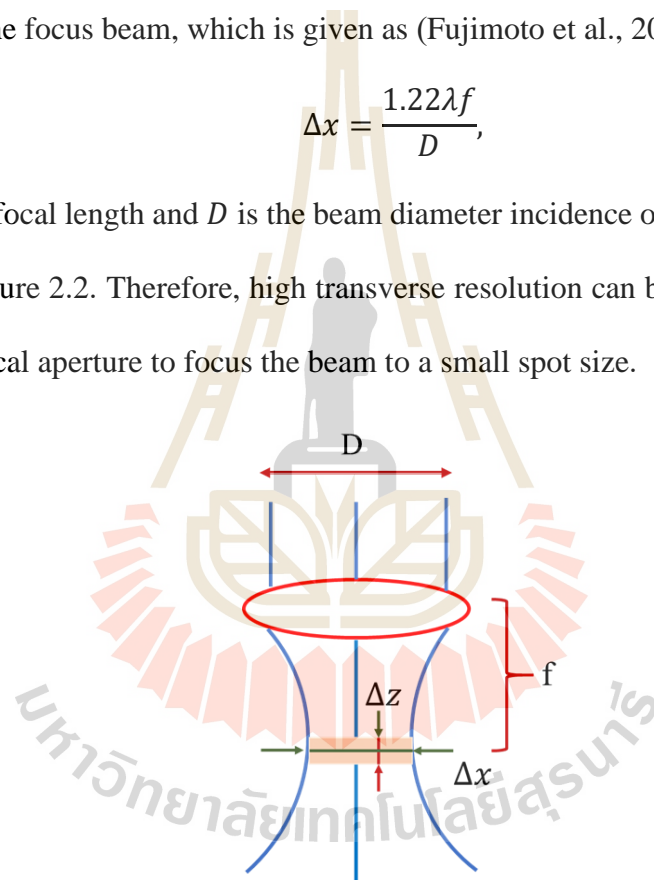


**Figure 2.2** Schematic diagram shows axial and transverse resolution of OCT system.

## 2.2 Spectral domain OCT (SD-OCT)

SD-OCT can be separated into two main setups depending on light source and detection system, which are swept-source based SD-OCT or swept-source OCT (SS-OCT) and spectrometer based SD-OCT. SS-OCT uses a broadband swept-frequency light to illuminate the sample as shown in Figure 2.3. The interference signal can be detected by using the single element detector (i.e. photodetector) to acquire the time-encode information of the interference spectra. The spectrometer based SD-OCT use the broadband light source to illuminate the sample and replace the detection part from single photodetector to the dispersive element (i.e. grating) and a linear photodetector array as shown in Figure 2.4. In both cases, fiber-based Michelson interferometer setup is commonly used (Fercher et al., 1995; Wojtkowski et al., 2002).

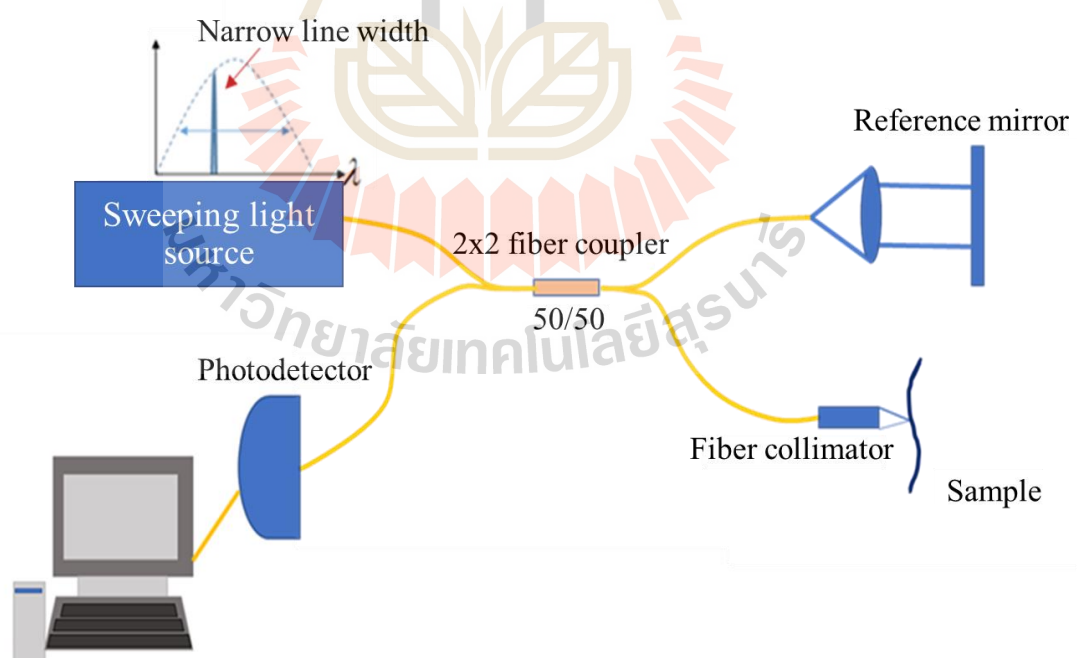


**Figure 2.3** Typical configurations of swept-source based SD-OCT.

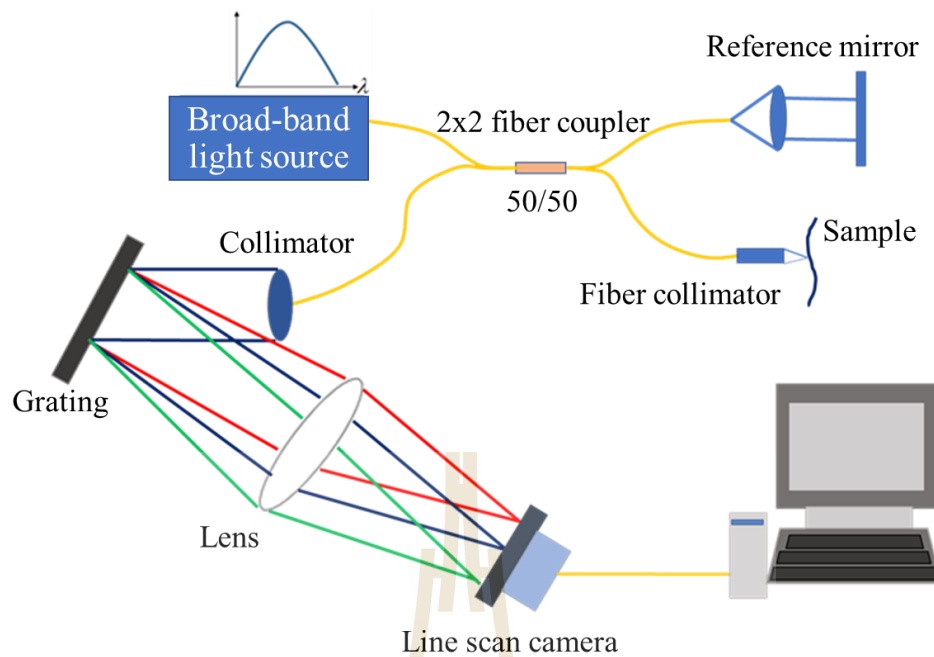


**Figure 2.4** Typical configurations of spectrometer based SD-OCT.

According to the SS-OCT, the high-speed frequency swept light source is normally high cost as compared to a high performance broadband light source. In addition, the high speed SS-OCT system needs to transfer more digitized data samples of the time-encoded interference spectra to the computer, which requires a high speed and high performance analog to digital converter module that is also relatively high cost as compared with a commercial high performance line-scan camera. Therefore, spectrometer-based SD-OCT is more suitable for a low-cost solution of SD-OCT imaging.

SD-OCT can be understood by recalling that a Michelson interferometer acts like a periodic frequency filter, where the periodicity is a function of the path difference between the sample and reference arms. From Figure 2.4, the output from a broadband light source is split into two beams. One beam is directed onto the tissue to be imaged and is back-reflected or back-scattered from internal structures at different

depths. The second beam is reflected from a reference mirror whose position is fixed. The sample beam and the reference beam have a relative time delay determined by the path length difference, which is related to the depth of the structure in the tissue. The interference of the two beams will have a spectral modulation as a function of frequency, which can be measured using a spectrometer. The periodicity of this modulation will be inversely related to the OPD. Therefore, different OPD will produce different frequency modulations. The depth reflectivity profile can be determined from the Fourier transformation of the spectral interference signal. This results in an axial scan measurement of the magnitude and echo delay of the light signal from different depth within the tissue (Fercher et al., 1995).

### 2.3 Mathematical description of SD-OCT

To describe the interference spectrum in SD-OCT system, we again consider the typical setup of SD-OCT as in Figure 2.4. The spectral electric field traveling from reference path can be expressed as

$$\hat{E}_R(k) = K_R \hat{E}_0(k) r_R \exp(jkl_R), \quad (2.3)$$

where  $k = \frac{2\pi}{\lambda}$  is the wave propagation number,  $\hat{E}_0(k)$  is the spectral electric field emitted by broadband light source,  $K_R$  is the total losses in the reference arm,  $r_R$  is the reflectivity of the reference reflecting element, and  $l_R$  is a round-trip propagation distance along the reference arm. On the other hand, the spectral electric field that back-scattered from the sample through the sample arm optics can be defined as

$$\hat{E}_S(k) = K_S \hat{E}_0(k) \int_{-\infty}^{\infty} r_S(l_S) \exp(jkl_S) dl_S, \quad (2.4)$$

where  $K_s$  is the total losses along the sample arm,  $l_s$  is the round-trip propagation distance along the sample arm,  $r_s(l_s)$  is the reflectivity profile at different depth of the sample as a function of  $l_s$  (Wang and Wu, 2007).

The signal that detected by the photodetector can be expressed in term of the intensity of the superposition of the sample and reference spectral electric fields as

$$\hat{I}_D(k) = |\hat{E}_R(k) + \hat{E}_S(k)|^2, \quad (2.5)$$

$$\hat{I}_D(k) = \hat{E}_R(k)\hat{E}_R^*(k) + \hat{E}_S(k)\hat{E}_S^*(k) + \hat{E}_S(k)\hat{E}_R^*(k) + \hat{E}_R(k)\hat{E}_S^*(k), \quad (2.6)$$

where  $\hat{E}_R^*$  and  $\hat{E}_S^*$  are the complex conjugate of the reference and sample spectral electric fields, respectively.

The equation (2.6) can be separated into three terms. The first term is

$$\hat{E}_R(k)\hat{E}_R^*(k) = K_R^2 |\hat{E}_0(k)|^2 r_R^2, \quad (2.7)$$

which is a static signal measured by blocking the sample arm and can be removed by direct subtracting. The second term is

$$\hat{E}_S(k)\hat{E}_S^* = |\hat{E}_0(k)|^2 \left| K_s \int_{-\infty}^{\infty} r_s(l_s) \exp(jkl_s) dl_s \right|^2, \quad (2.8)$$

which represents the auto-correlation term (AC-term) that is the interference of all of the backscattered light from the sample itself. This term is normally much smaller than the signal from the first term and third term (i.e.  $r_s \ll r_R$ ). Therefore, it can be ignored or can be removed by blocking the reference arm then taking the subtraction. The third term is

$$\hat{E}_S(k)\hat{E}_R^* + \hat{E}_R(k)\hat{E}_S^*(k) = 2K_R K_s |\hat{E}_0(k)|^2 r_R \int_{-\infty}^{\infty} r_s(l_s) \cos(k(l_s - l_R)) dl_s, \quad (2.9)$$

which represents the interference between sample and reference arm. By setting the optical path difference to  $l_D = l_s - l_R$  and assuming the DC and AC term can be removed, the interference spectrum can be rewritten as

$$\hat{I}_{int}(k) = 2K_R K_S r_R S(k) \int_{-\infty}^{\infty} r_s(l_D) \cos(kl_D) dl_D, \quad (2.10)$$

where  $S(k) = |\hat{E}_0(k)|^2$  is the power spectrum intensity of the light source, and  $r_s(l_D)$  is the sample reflectivity along the optical path difference  $l_D$ . In addition, consider the cosine term as the exponential function, the equation (2.10) can be rewritten as

$$I_{int}(k) = K_R K_S r_R S(k) \left[ \int_{-\infty}^{\infty} r_s(l_D) \exp(jkl_D) dl_D + \int_{-\infty}^{\infty} r_s(l_D) \exp(-jkl_D) dl_D \right], \quad (2.11)$$

From the Fourier transform of the space variable as

$$\mathfrak{F}\{f(x)\} = \int_{-\infty}^{\infty} f(x) \exp(-jkx) dx, \quad (2.12)$$

and using its property as  $\mathfrak{F}\{f(-x)\} = F(-k)$  equation 2.11 can be rewritten as

$$I_{int}(k) = K_R K_S r_R S(k) \left[ \mathfrak{F}\{r_s(-l_D)\} + \mathfrak{F}\{r_s(l_D)\} \right]. \quad (2.13)$$

Consequently, the inverse Fourier transform of the product of two functions in equation (2.13) yields

$$I_{OCT}(l_D) = K_R K_S r_R \mathfrak{F}^{-1}\{S(k)\} * [r_s(-l_D) + r_s(l_D)], \quad (2.14)$$

From equation (2.14), a depth-resolved reflectivity profile of the sample or an OCT signal can be obtained from the inverse Fourier transform of the detected interference spectrum. For example, assume the homogenous multi-layered materials as the sample that the reflectivity is the delta function at the different depth and refractive index. The  $\mathfrak{F}^{-1}\{S(k)\}$  represents the axial point spread function for creating the resolved depth profile by the convolution along the symmetry function of the sample reflectivity that is  $r_s(-l_D)$  and  $r_s(l_D)$  as shown in Figure 2.5.

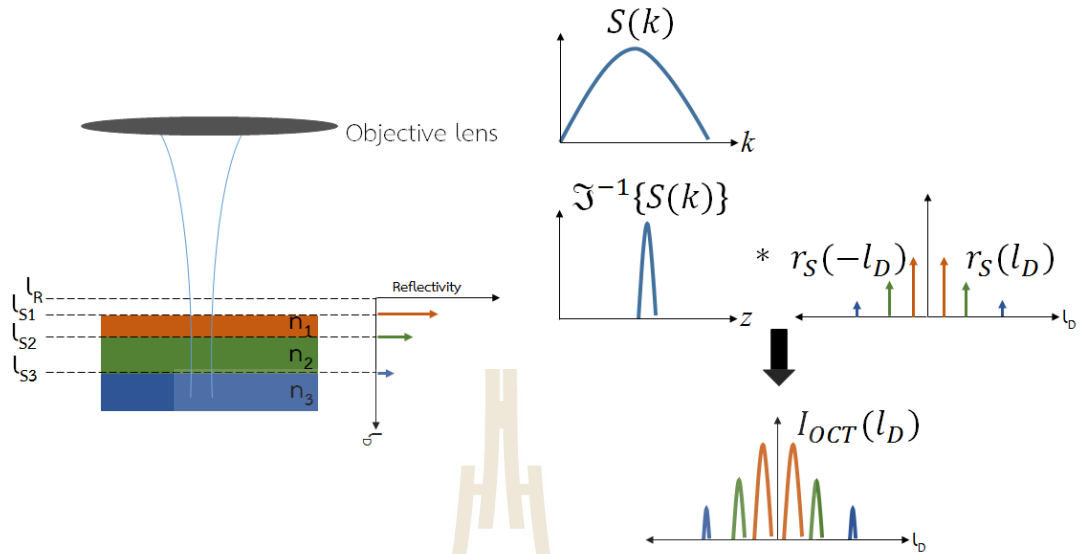


**Figure 2.5** Illustration of the depth-resolved reflectivity profile obtained from inverse Fourier transform of the interference spectrum.

Because of the Fourier transform relation, the maximum imaging depth of SD-OCT ( $Z_{max}$ ) is limited by the wavelength spacing between pixels ( $\delta\lambda$ ) of the spectrometer, which is determined by either the pixel size of the sensor or the optical resolution of the focusing optics of the spectrometer (Lee et al., 2009). From equation of angular wave number

$$k = 2\pi\xi = \frac{2\pi}{\lambda}, \quad (2.15)$$

Divide equation (2.15) by  $2\pi$  and take derivative by  $\lambda$  yield

$$\frac{d\xi}{d\lambda} = \frac{d}{d\lambda} \left( \frac{1}{\lambda} \right), \quad (2.16)$$



$$d\xi = \frac{-1}{\lambda^2} d\lambda. \quad (2.17)$$

The negative sign can be interpreted as opposite direction between frequency space and wavelength space, i.e. the flipping of spectrum shape as show in Figure 2.6(A). From

Figure 2.6(A), substituting  $d\lambda = \frac{\Delta\lambda}{N_{sensor}}$  into equation (2.17) yields

$$d\xi = \frac{-d\lambda}{\lambda^2} = \frac{-\Delta\lambda}{\lambda^2 N_{sensor}}. \quad (2.18)$$

From Figure 2.6(B), the total range in spatial domain is

$$Z = \frac{1}{d\xi}. \quad (2.19)$$

Substituting equation (2.18) into equation (2.19) yields

$$Z = -\frac{\lambda^2 N_{sensor}}{\Delta\lambda}. \quad (2.20)$$

From Figure 2.6(B), the maximum imaging range of SD-OCT can be defined by

$$Z_{max} = \frac{1}{2} |Z|, \quad (2.21)$$

$$Z_{max} = \frac{1}{2} \left| \frac{\lambda^2 N_{sensor}}{2\Delta\lambda} \right|. \quad (2.22)$$

Multiply Equation (2.22) by 1/2 for a round trip propagation and multiply 1/n when consider sample refractive index, Equation (2.22) becomes

$$Z_{max} = \left| \frac{\lambda^2 N_{sensor}}{4n\Delta\lambda} \right|, \quad (2.23)$$

where  $\Delta\lambda$  is a full spectral bandwidth,  $\lambda$  is a center wavelength and  $N_{sensor}$  is the total pixel number of the line-scan camera.

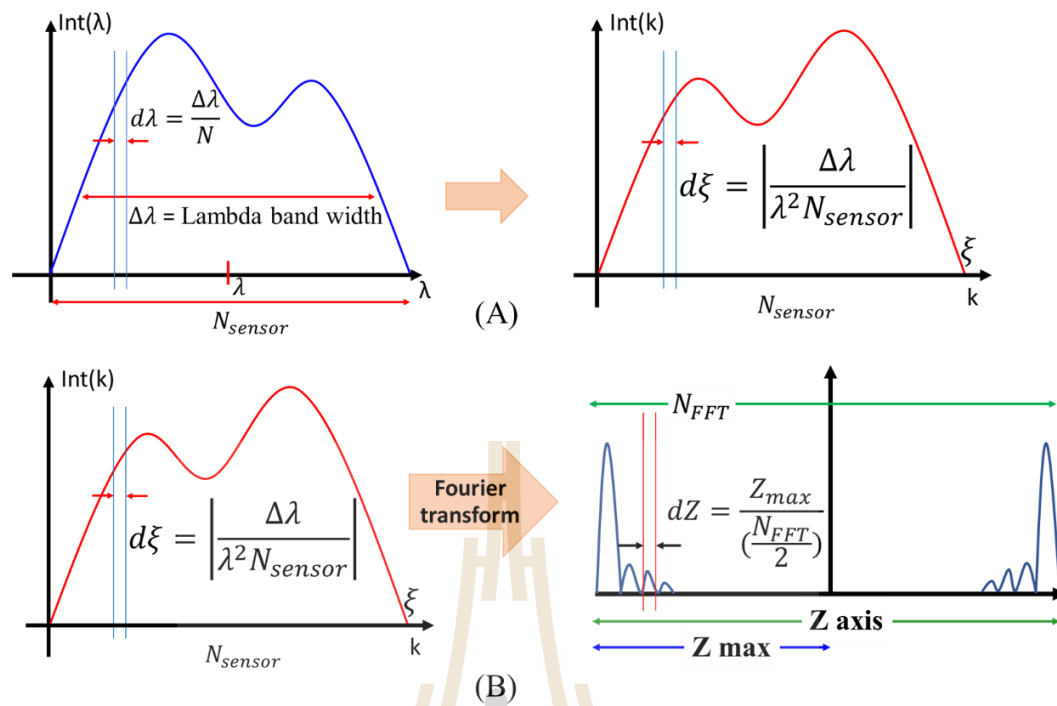


**Figure 2.6** (A) Examples of a broadband spectral signals as a function of  $\lambda$  and  $\xi$  (B) Reflectivity profile as a function of depth location is a Fourier transform of spectral interference, where  $\lambda$  is center wavelength,  $\Delta\lambda$  is a full spectral bandwidth,  $N_{\text{sensor}}$  is the total pixel number of the line-scan camera,  $N_{\text{FFT}}$  is a number of pixels after the fast Fourier transform, and  $Z_{\text{max}}$  is maximum imaging depth of SD-OCT.

As shown in equation (2.23) the depth of imaging performance of SD-OCT is depended on the spectral resolution of its spectrometer system. Table 1 shows the specification of the spectrometer design for SD-OCT that has been developed and presented.

Table 2.1 Examples of recent development of spectrometer-based SD-OCT.(An et al., 2011; Fan et al., 2007; Grulkowski et al., 2009; Lee et al., 2009; Xi et al., 2011).

Author/Year	Spectrometer					Maximum	Axial
	$\lambda_0(nm)$	$\Delta\lambda(nm)$	Camera type	pixels	line rate	imaging depth(mm)	resolution ( $\mu m$ )
1. Sang-Won Lee et al. (2009)	1300	170	InGaAs	1024	46.99 k lines/s	2	8.2
2. Ireneusz Grulkowski et al. (2009)	840	50	CMOS	4096	135 k lines/s	5.2	6.9
3. Peng Xi et al. (2011)	840	40	CCD	1024	24k lines/s	2	7.7
4. Fan et al. (2007)	850	40	CCD	1024	10 k lines/s	3	10
5. Lin An. (2011)	850	Not available	CMOS	800	500 k lines/s	2.5	8

## 2.4 Spectrometer design for SD-OCT

There are two main typical designs of the grating-based spectrometer to use in SD-OCT, which requires the high-speed, high-sensitivity, and high resolution to resolve the highest modulation frequency of the interference spectra. The first design is lenses-based grating spectrometer as shown, for example, in Figure 2.7(A). The second is mirrors-based grating spectrometer or Czerny-Turner spectrometer as shown, for example, in Figure 2.7(B) (Czerny and Turner, 1930). The main important components of both setups consist of a collimating element to make the beam shape parallel along to the optical axis to the grating and a focusing element to focus the collimated wavelength dispersed light from grating onto a line array photodetector, such as a line-scan camera.

The lenses-based grating spectrometer uses lenses that possess the chromatic aberrations. As compared with the speed of light in free space, the speed of light in a medium is inverse proportional to the refractive index of the medium. Therefore, caused by the dispersion of the material, different wavelengths of light travels at different speeds inside a medium. As a result, the dispersion of the lens causes different wavelengths to be focused at different positions across the focal plane and along the optical axis, which known as 'chromatic aberration', that degrades the resolution of the lens. Even though the chromatic aberration can be optimized, it could be challenging for the high-resolution spectrometer.

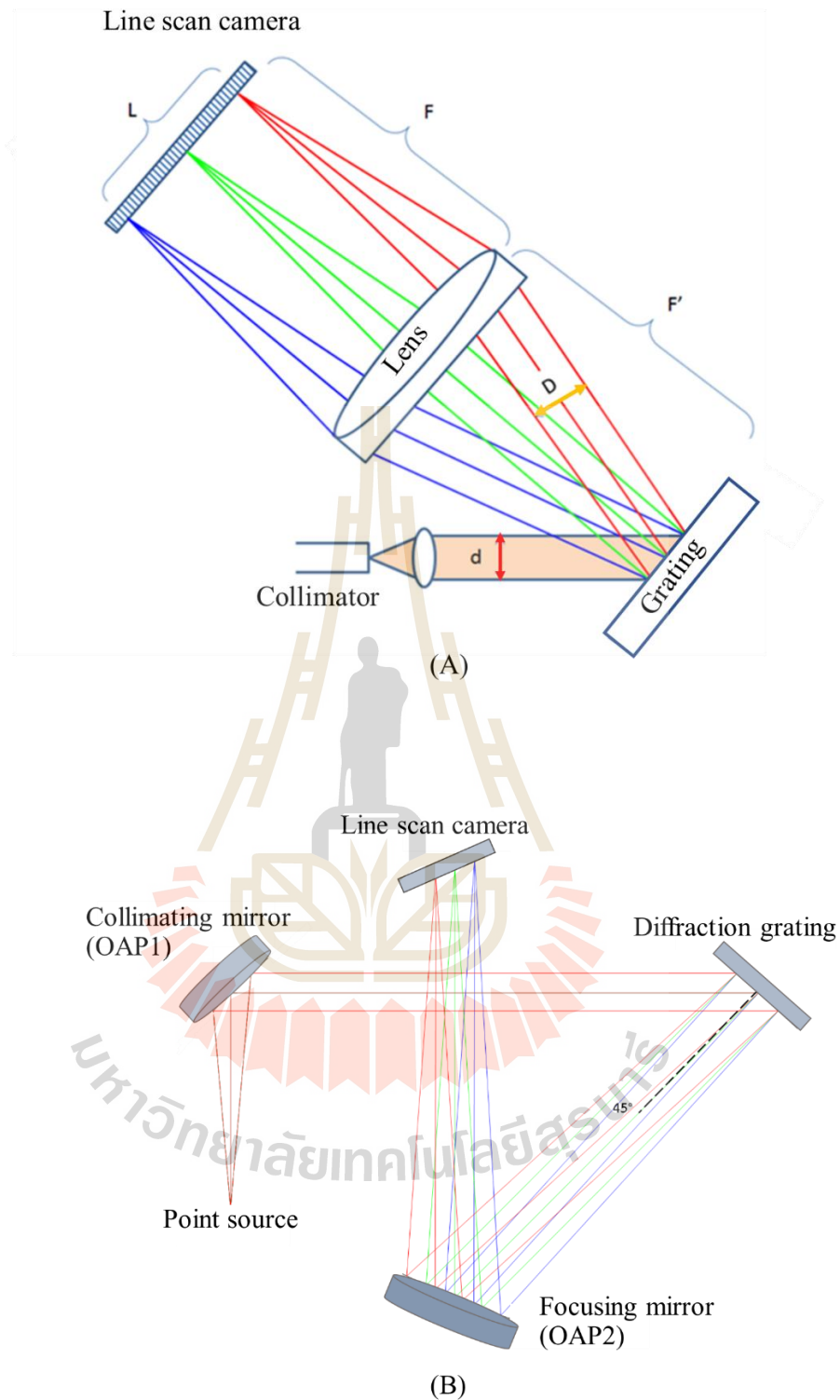


**Figure 2.7** Typical configurations of grating spectrometer setup of (A) lenses-based grating spectrometer and (B) mirrors-based grating spectrometer.

In addition, the spherical shape of the lens will affect the focusing spot point as well. This is because, when light travels at the near edge of the spherical lens, the refraction increases as compared with that strike near the center of the lens, which is called ‘spherical aberration’. The aberrations will reduce the spectrum resolving power of the detected interference spectrum of the broadband light source that degrades the resolution and sensitivity of SD-OCT system. However, the setup and the optical alignment of the lenses-based grating spectrometer is not much complicate and therefore is suitable for typical SD-OCT system (An et al., 2011; Meemon et al., 2014) if the used light source is not an extremely wide bandwidth.

Given that light travels to the reflective surfaces does not affect by dispersion, the Czerny-Turner spectrometer focuses the light beam by using spherical mirrors to avoid the effect of the chromatic aberration, which is more suitable for wide bandwidth light source (Czerny and Turner, 1930). However, spherical mirrors still possess spherical aberration that could limit the resolution of the spectrometer. The use of a low numerical aperture can reduce the effect of the spherical aberration. However, the low numerical aperture system will lead to larger diffraction spot size as determined by

$$\Delta x = 0.61 \frac{\lambda}{NA} = 1.22\lambda \frac{f}{D}, \quad (2.24)$$

where  $NA$  is the numerical aperture of the focusing optics,  $\Delta x$  is the spot size resolution that is focused at the sensor,  $f$  is focal length of focusing optic, and  $D$  is the beam size after disperse from the diffraction grating that must be less than the size of the grating.

As a result, the spectral resolution of better than 0.1 nm is difficult to achieve. Lee K. et al. (2009) review the Czerny-Tuner spectrometer aberrations and take the astigmatism correction by adding the cylindrical lens in front of the line-scan camera for using with a wide bandwidth light source, which improves the spectral resolution

better than 0.1 nm of SD-OCT system. The Czerny-Turner spectrometer is typically used in the desired of high axial resolution SD-OCT system (Lawman et al., 2016; Yadav et al., 2011). However, this design requires precise optical alignment to adjust the tilted angle of each mirrors, which is used in the off-axis geometrical configuration that is much more complicated to determine the focal plane of the system.

## 2.5 Modulation transfer function (MTF)

MTF is the spatial frequency response of an imaging system or a component. MTF is a measure of the modulation contrast of the oscillating signal amplitude at a given spatial frequency relative to low frequencies (Woolliams and Tomlins, 2011). To understand the concept of the MTF, we shall consider the different periods of black and white bars with 50% duty cycle. An image of the bars is a convolution between the bars and the point spread function of the imaging system. As the bars become closer together, the image starts to become more and more blurry. Mathematically, the percent contrast can be calculated by

$$\%contrast = \left[ \frac{I_{max} - I_{min}}{I_{max} + I_{min}} \right] \times 100. \quad (2.25)$$

The MTF plot as a function of the spatial frequency represents the contrast of modulation of the image as compared to an ideal image as shown in Figure 2.8

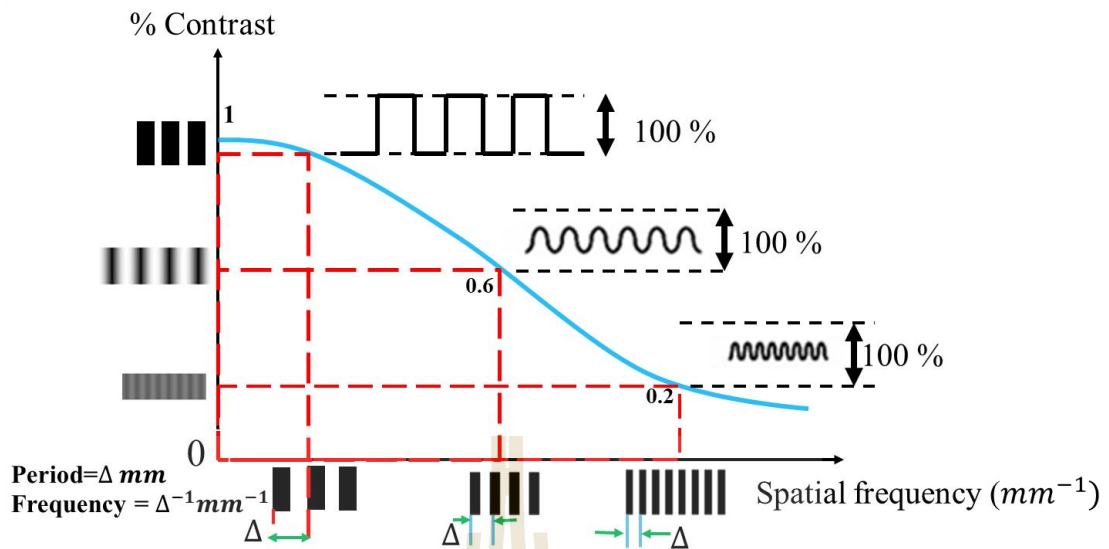


**Figure 2.8** Modulation transfer function (MTF) graph.

For example, the minimum intensity is 0 where it's black and the maximum intensity is 1 where it's completely white. The modulation is computed to be 100% in this case. However, the spatial frequency becomes higher as the bars period gets smaller. The captured image will not be perfectly black and white bars anymore and the modulation will be less than 100% as shown in Figure 2.8. Eventually, at high enough frequency, the MTF drop to 0.

Whilst PSF width is widely used within the OCT literature as an instrument metric, a more widely accepted measurement of image quality is the modulation transfer function (MTF). The direct measurement of the PSF is not suitable for alignment of a spectrometer for SD-OCT. On the other hand, using the principle of spectral interference, it is more convenient to produce modulated spectral signal on the sensor of the spectrometer that can be used to quantify modulation contrast of the focusing optics of the spectrometer. This would allow for direct MTF measurement of the spectrometer during its alignment process.



## **CHAPTER III**

### **METHODS**

#### **3.1 MTF measurement technique**

To allow for the verification of the resolution performance of a spectrometer during its alignment process, we have developed a technique to quantify MTF performance on different region of a line array sensor of the spectrometer. In this developed technique, the amplitude modulated spectrum was produced by using a free-space low-coherence interferometer (LCI). Based on the interference theorem, interference of two broadband light beams appears as modulated spectrum in the frequency domain (M. Born and E. Wolf, 1999). Moreover, the modulated frequency of the signal is associated with the optical path delay (OPD) between the two beams. The longer the OPD, the higher the frequency of the spectral interference. As a result, the modulation frequency of the spectral interference signal is fully controllable.

In this experiment, we used a free-space Michelson interferometer as shown in Figure 3.1 to produce an amplitude modulated spectrum to be put into the implemented spectrometer. The modulated frequency can be varied by changing the OPD between the two beam paths of the interferometer, i.e. by translating the movable mirror along its beam path as designated in Figure 3.1. The relation between the translated distance of the movable mirror and the produced modulation frequency on the spectral interference can be predetermined.

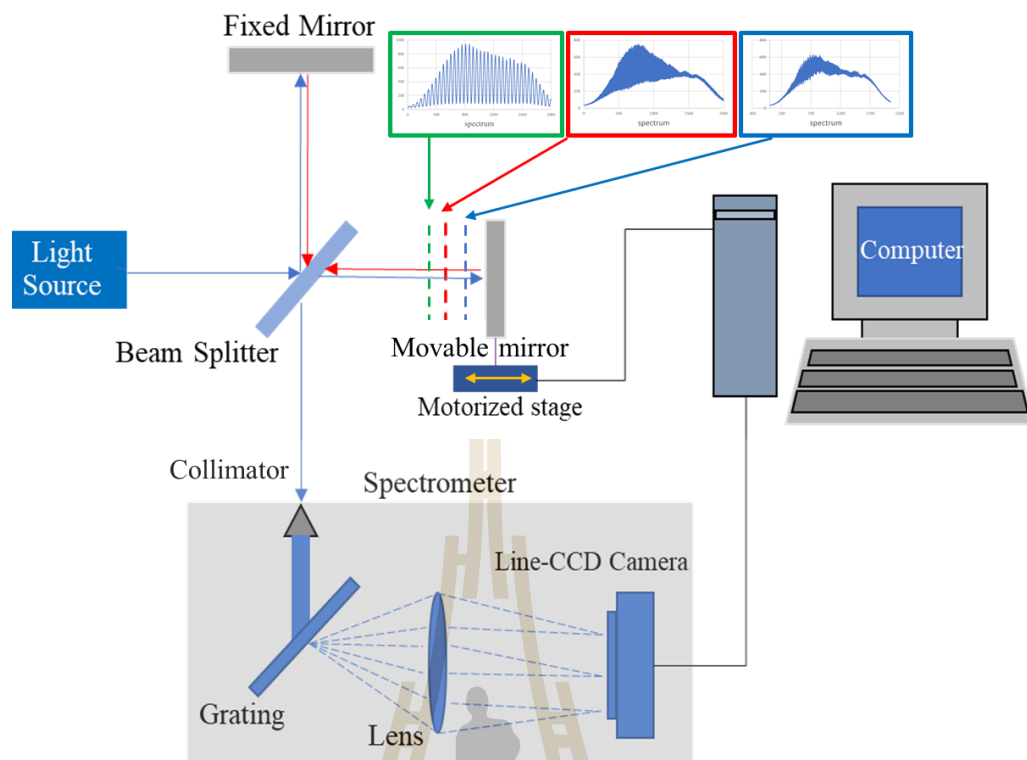


**Figure 3.1** The layout of a Michelson interferometer setup for the MTF measurement of the spectrometer.

Figure 3.2 shows a photograph of the experimental setup for the MTF measurement of the spectrometer, which consisted of fixed mirror, moveable mirror, beam splitter, collimator, and light source. The light emitted from the light source was collimated and split into two beams by a beam splitter. The first beam reflected from the beam splitter, was incident on the fixed mirror, reflected back and transmitted through the beam splitter, coupled to a single mode fiber, and delivered to the spectrometer under tested. The second beam transmitted through the beam splitter, was incident and reflected on the movable mirror, reflected at the beam splitter, and coupled to the same single mode fiber. The spectrometer captures the interference of the two beams, i.e. the spectral

interference, whose frequency can be changed by changing the optical path difference (OPD) by translating the movable mirror along the beam path.

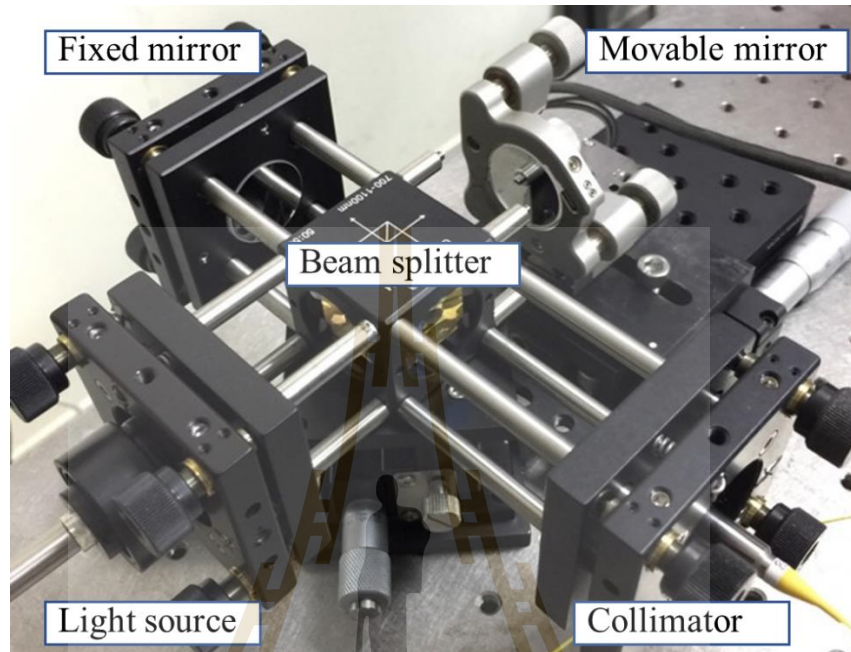


**Figure 3.2** The photograph of the LCI setup for the MTF measurement.

Furthermore, the MTF performance of sub-region of the line array-sensor can be separately determined. For example, as shown in Figure 3.3, the detected modulated spectrum is divided into 5 zones. A raw data of modulated spectrum obtained directly from the spectrometer is subject to a non-uniform modulation amplitude that causes by the spectrum shape, i.e. a non-uniform spectral weight of the light source. The effect of the spectrum shape can be suppressed by dividing the raw modulated spectrum by its non-modulated version as will be detailed in Section 3.2. From the adjusted modulated spectrum, the average modulation contrast of each zone can be computed using the equation as shown in the figure, where  $I_{\max}$  and  $I_{\min}$  are averaged values of peaks and valleys, respectively, of the modulated signal in each zone. The process is repeated for

the modulated spectra obtained at different modulation frequencies to produce an MTF curve for each zone.

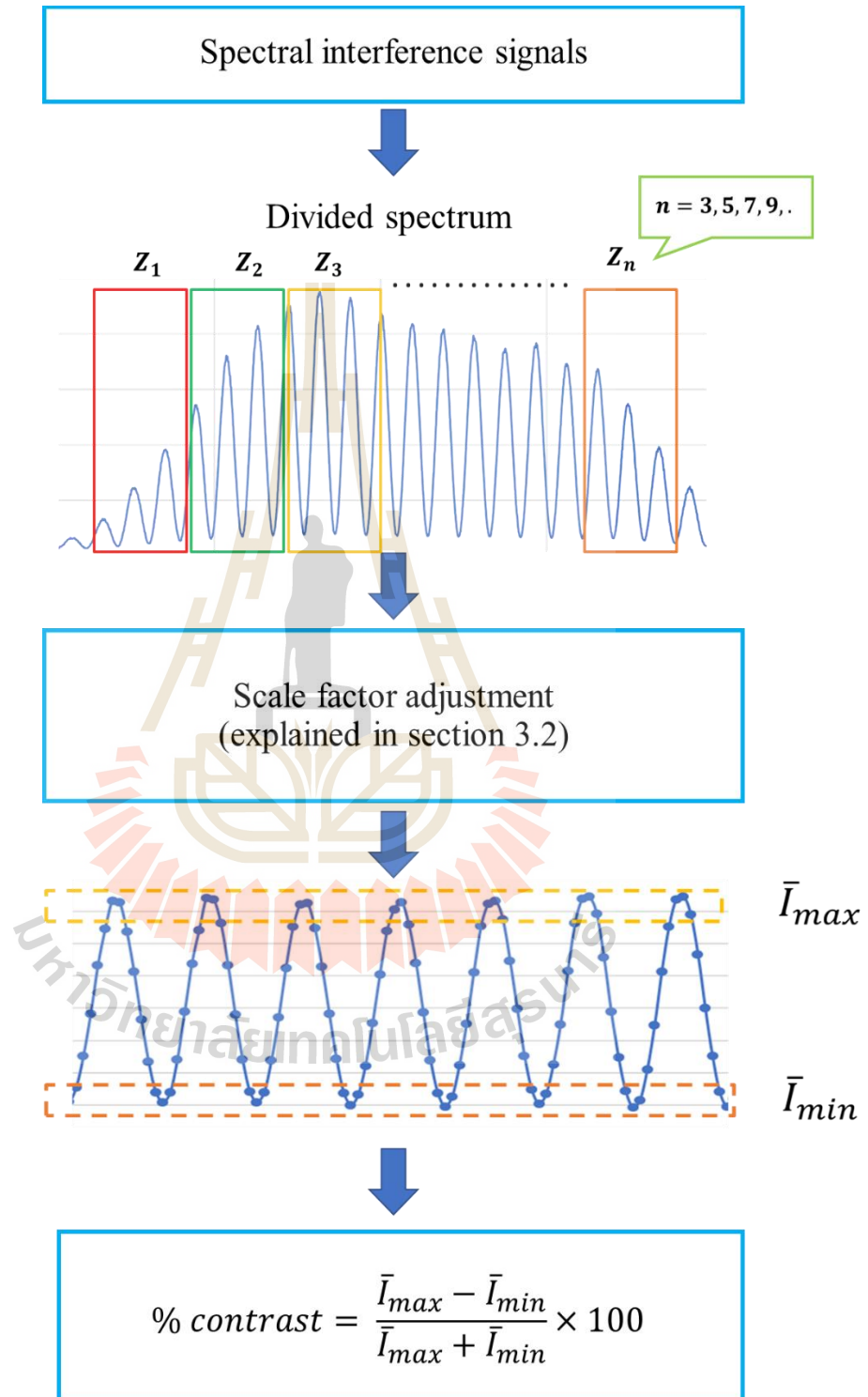


**Figure 3.3** The procedure of MTF calculation.

### 3.2 Spectrum shape adjustment

The non-uniform amplitude of the measured modulated spectrum will lead to difficulty in determination of the modulation contrast at the edge of the sensor area. This shape factor can be minimized by subtracting the raw modulated spectrum by the non-modulated spectrum data. The non-modulated spectrum can be obtained by the summation of the two spectra, one from the fixed mirror arm and the other from the movable mirror arm. Figure 3.5 show a few examples of the scale factor adjustment of modulated spectra obtained at different modulation frequencies.

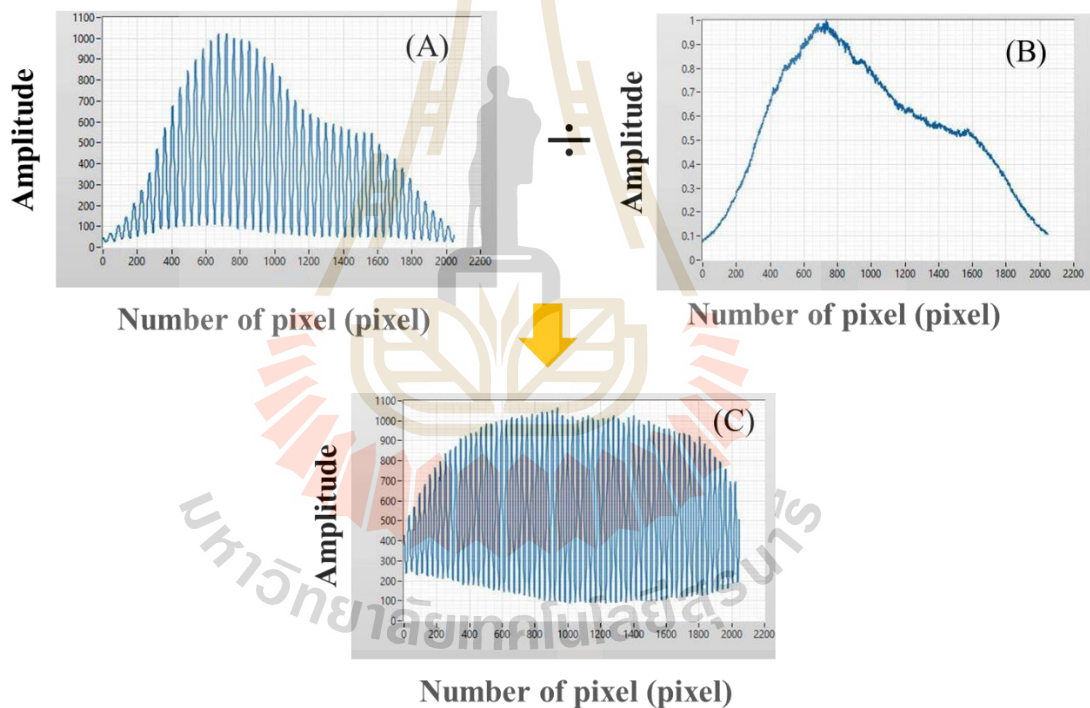


**Figure 3.4** The scale factor adjustment can be performed by dividing (A) The modulated spectrum with (B) the non-modulated spectrum of the light source to obtain (C) a uniform modulation amplitude across the sensor region.

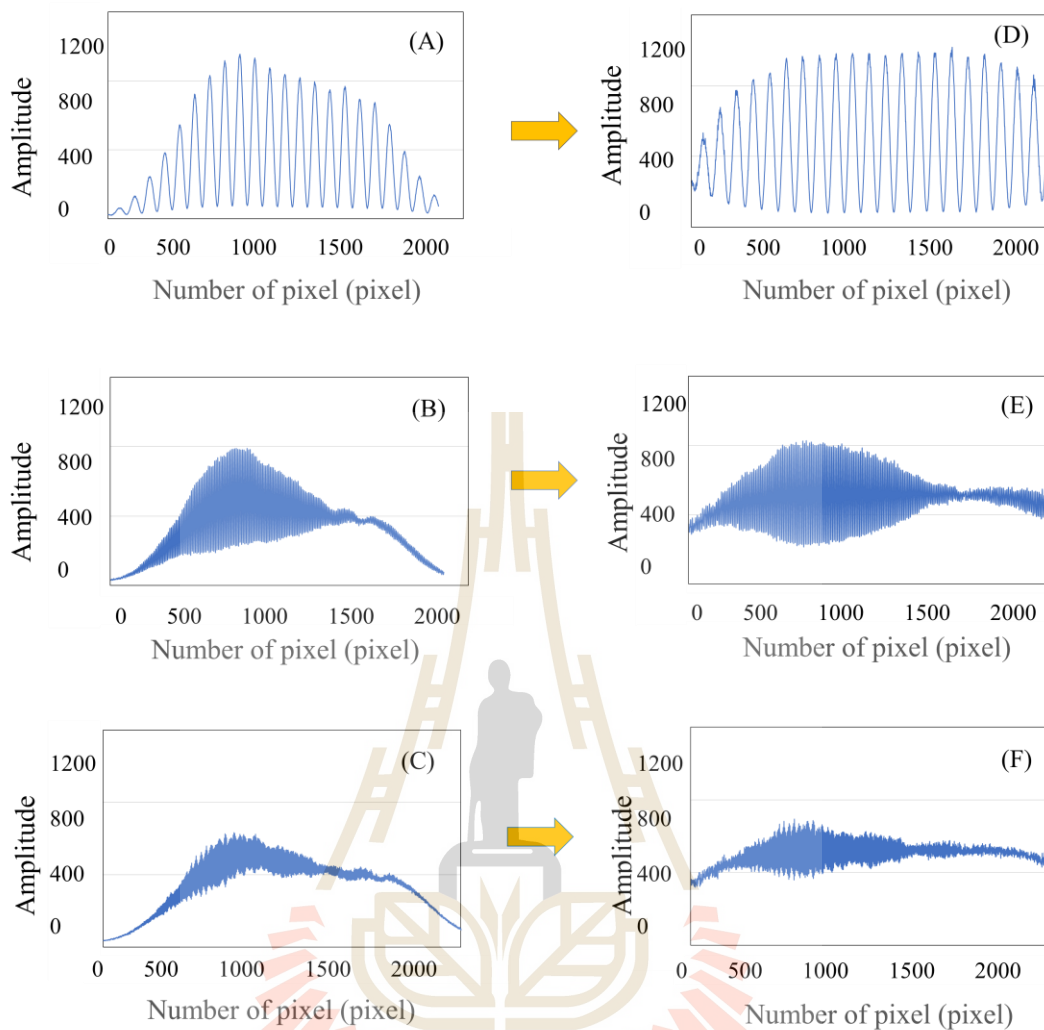


**Figure 3.5** (A-C) The spectrum obtained at different modulation frequencies and the spectrum that can be detected to be divided by data that normalize will get a new shape spectrum as shown in Figure (D-F).

### 3.3 Spectrometer design and implementation

#### 3.3.1 Lenses based spectrometer

In this experiment, a simple spectrometer design was implemented, consisting of a fiber collimator, a reflective grating, a focusing lens, and a line array-sensor. The spectrometer was design for using with a broadband super-luminescent diode (SLD)

light source (S-840-B-I-20, Superlum, Inc., Ireland) with a central wavelength ( $\lambda_0$ ) of 840 nm and a full spectral range of about 90 nm as shown in Figure 3.6(A). A CMOS based line-array sensor (ral 4096-80km, Basler Vision Technologies, Germany) was chosen as the detector. The sensor consists of a line of CMOS array with 4,096 pixels per line and with  $7 \mu\text{m} \times 7 \mu\text{m}$  pixel size. The sensor is capable of high speed of signal capturing and data transfer to a computer of up to 80,000 lines per second for a full 4096 pixels per lines and 12 bits resolution, which has great potential for high speed SD-OCT.

To achieve high spectral resolution, a grating with a high groove density of 1200 lines/mm (i.e. grating spacing of  $0.83 \mu\text{m}$ ) was chosen. The grating provided sufficient dispersion power, i.e. 0.1 radian or approximately 5 degrees, for the targeted spectral width of the light source. A sketch design of the spectrometer is illustrated in Figure 3.6(B). After incidence on the grating, each wavelength of light will form a collimated beam incidents on the focusing lens at different field angles. This causes the focus of light laterally expands across the line sensor, i.e. a distance  $L$  between red and blue spots on the line array sensor as shown in Figure 3.6(B). The length  $L$  determines number of samples per spectrum of the spectrometer and serves as a sensor limit spectral resolution of the spectrometer.

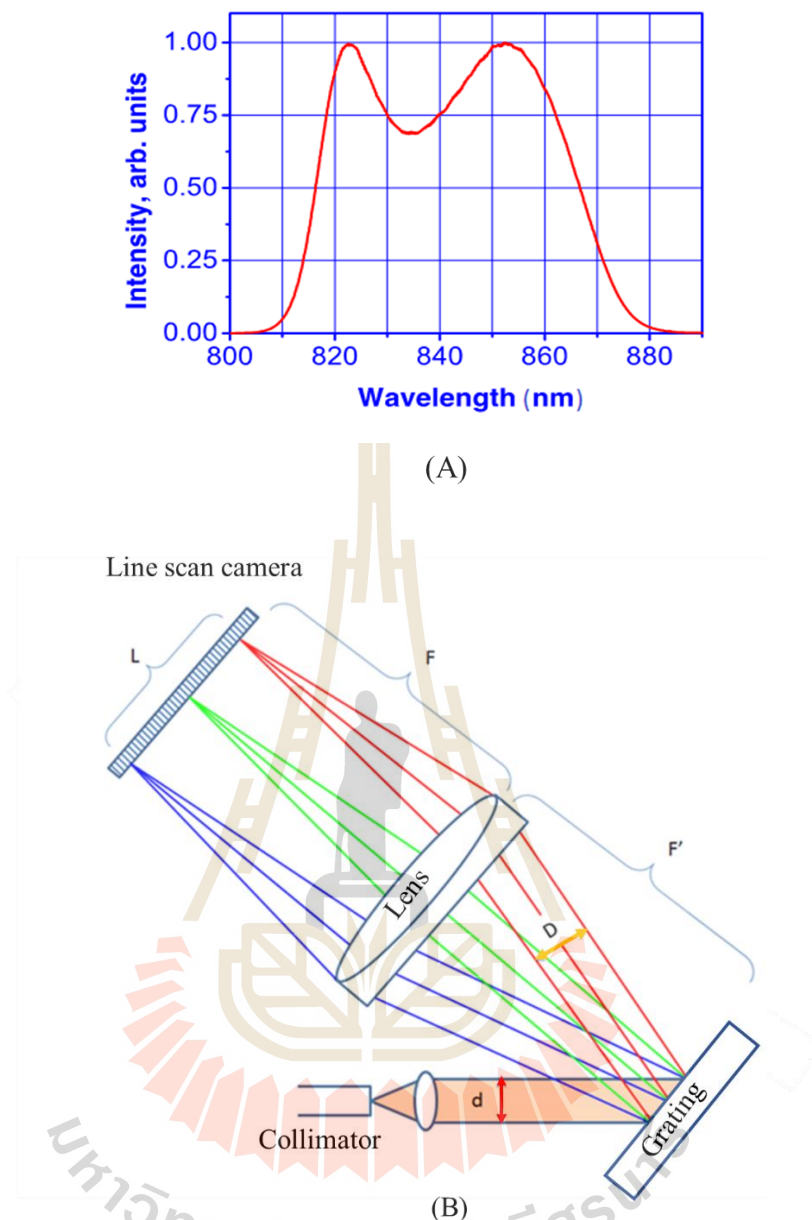


**Figure 3.6** (A) The power spectrum of the light source. (B) The optical design layout of the spectrometer.

In addition, from Figure 3.6(B), the size of the incident collimated beam will determine an optical limit focus spot on the sensor and eventually determine the spectral resolution of the spectrometer. In experimental setup, the overall aberration of an actual lens needs to be accounted for and would normally become an actual limiting factor of



the spectral resolution of the spectrometer. Ideally, a high-resolution spectrometer requires maximum  $L$  and minimum focus spot. Experimentally, these two parameters need to be traded-off to optimize the spectral resolution.

Based on the spectrometer design, we constructed a spectrometer in our laboratory using all off-the-shelf components. A commercially available large beam collimator of size 8 mm (F810APC-842, Thorlabs, USA) was used. The collimated light beam was then incident on a ruled diffractive grating, having a groove density of 1200 lines/mm (GR25-1208, Thorlabs, USA). The focusing optics was a combination of an achromatic doublet (AC508-075-B, Thorlabs, USA), having an effective focal length of 75 mm, and a concave lens (LC1315-B - N-BK7, Thorlabs, USA), having an effective focal length of -75 mm. The purpose of adding a concave lens is to maximize the length of the focal line. A set of spectra was captured by a CMOS line sensor (ral 4096-80km, Basler Vision Technologies, Germany) and then was transferred to a computer memory through a high speed frame grabber (NIPCIe-1433, National Instruments, USA). The spectrum capturing was controlled, processed, and displayed using LabVIEW software (National Instruments, USA).

### 3.3.2 Reflector based spectrometer

The spectrometer design was started from selecting the spot size resolution that must be less than the sensor pitch. The spectral image width is the image field-of-view at the focusing optics, which depends on both of focusing optics and the grating disperse angle. The spectrometer was design for using with a broadband super-luminescent diode (SLD) light source (EXS210088-02, EXALOS) with a central wavelength ( $\lambda_0$ ) of 880 nm and a full spectral range of about 120 nm as shown in Figure 3.7(A).

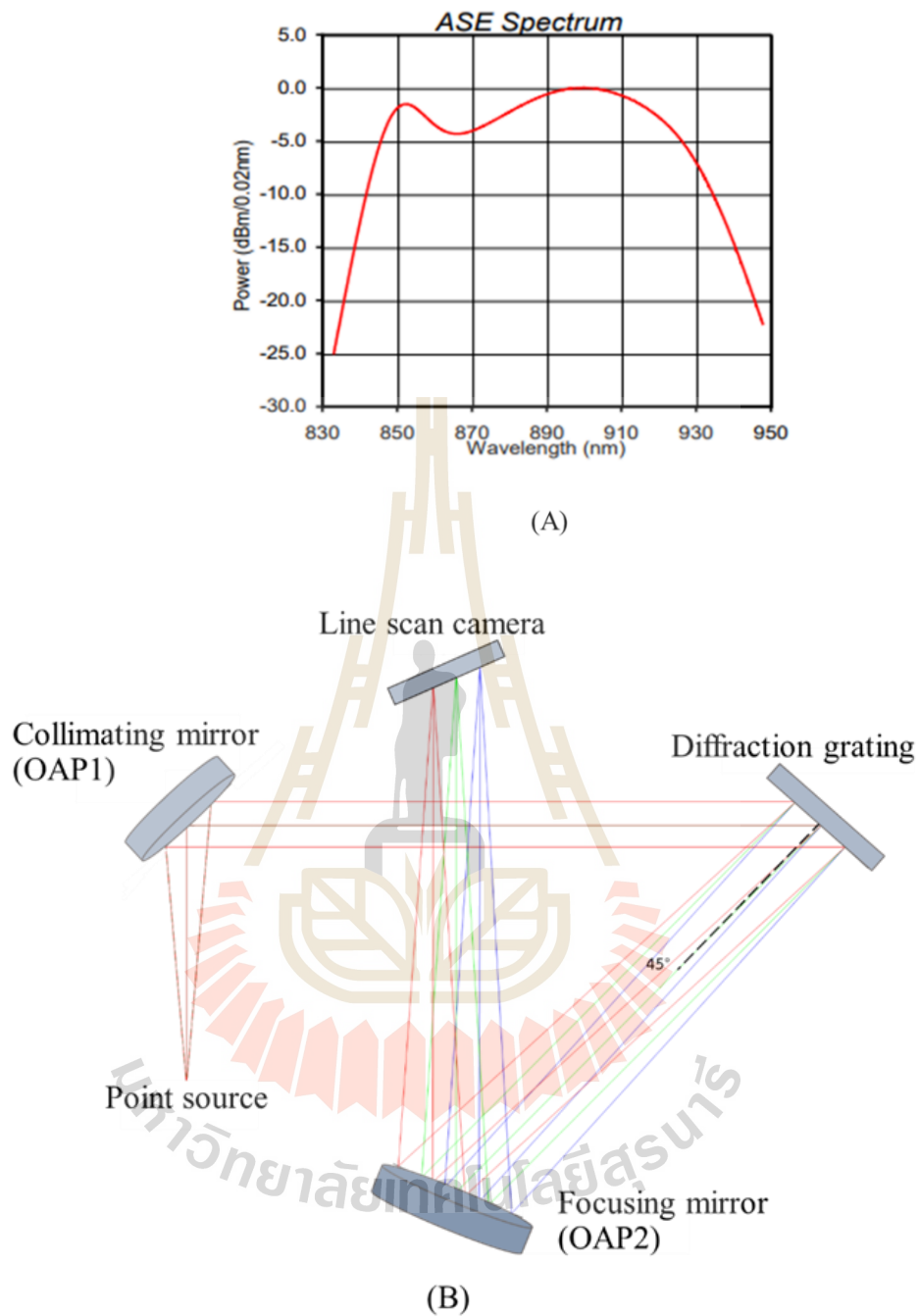


**Figure 3.7** (A) The power spectrum of the light source. (B) The optical design layout of the spectrometer.

The reflective spectrometer was designed and implemented as shown in Figure 3.7(B) consisting of a fiber collimator, a grating with a high groove density of 1200 lines/mm, an off-axis Parabolic Mirror with  $45^\circ$  off-axis and 203.2 mm focal length,

an off-axis Parabolic Mirror with 90° off-axis and 83.3 mm focal length, and a line array-sensor. A CMOS based line-array sensor (Mars2048-L51gm, Contrastech Co., Ltd.) was chosen as the detector. The sensor consists of a line of CMOS array with 2048 pixels per line and with  $10 \mu\text{m} \times 10 \mu\text{m}$  pixel size.

The resolution equation based-on the diffraction theory that can be expressed as below,

$$\Delta x = \frac{1.22\lambda f}{D}, \quad (3.1)$$

Where  $\Delta x$  is the spot size resolution that is focused on the sensor,  $f$  is focal length of focusing optics, and  $D$  is the beam size after being dispersed from the diffraction grating that must be less than the size of the grating.

We can obtain  $D$  from

$$D = \frac{d}{\cos\theta_i} = \frac{2 \times NA \times RFL}{\cos\theta_i}, \quad (3.2)$$

Where  $d$  is the collimated beam size after the light from the optical point source with numerical aperture  $NA$  reflect from the off-axis parabolic (OAP) mirror as collimator with the reflective focal length  $RFL$ .

### 3.4 Spatial frequency in cycles per millimeters

Both lens-based spectrometer and reflective spectrometer have the same limitations from the sensor. The highest possible resolvable frequency of both systems can be explained as show in Figure 3.8.

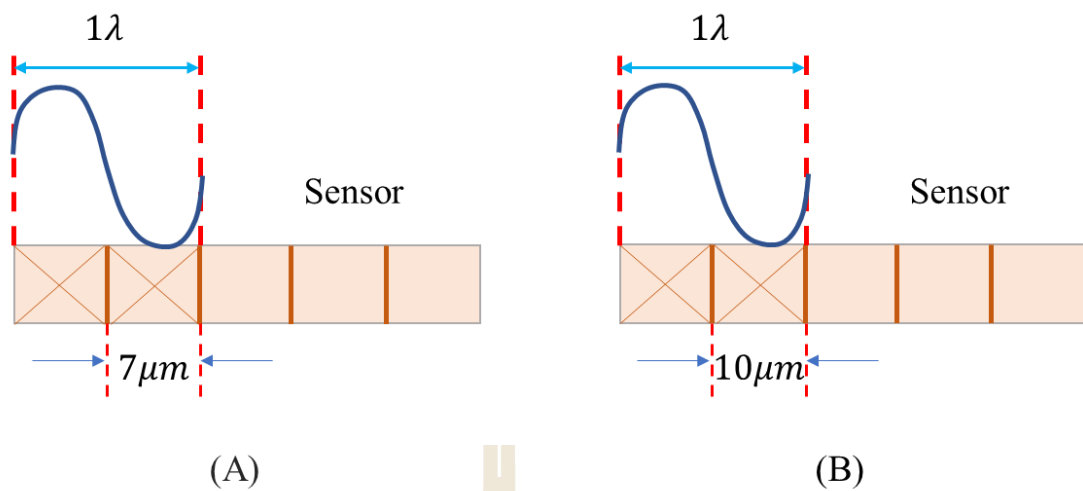


**Figure 3.8** Schematic limitations of the sensor of both systems.

For the lens-based spectrometer, the smallest resolvable cycle by the sensor corresponds with

$$1\lambda = 2 \text{ pixel/cy} \times 7\mu m/\text{pixel} , \quad (3.3)$$

$$1\lambda = 14\mu m/\text{cy} , \quad (3.4)$$

So, the minimum frequency that can be resolved by the sensor is

$$\xi_{max} = \frac{1}{14} \text{ cy}/\mu m, \quad (3.5)$$

$$\xi_{max} = 70 \text{ cy}/mm. \quad (3.6)$$

Diffraction limit resolution of the lenses based spectrometer, can be computed using equation (3.1) as

$$\Delta x = \frac{1.22 \times (840 \times 10^{-9}m) \times 75 \times 10^{-3}m}{8 \times 10^{-3}m}, \quad (3.7)$$

$$\Delta x = 9.6 \mu m \approx 10 \mu m. \quad (3.8)$$

So, the maximum frequency of the systems is  $\xi = 50 \text{ cy/mm}$ . Therefore, the system is limited by the focus spot.

And for the reflective spectrometer, the smallest resolvable cycle by the sensor corresponds with

$$1\lambda = 2 \text{ pixel/cy} \times 10\mu\text{m/pixel}, \quad (3.9)$$

$$1\lambda = 20\mu\text{m/cy}, \quad (3.10)$$

So, The minimum frequency that can be resolved by the sensor is

$$\xi_{max} = \frac{1}{20} \text{ cy}/\mu\text{m}, \quad (3.11)$$

$$\xi_{max} = 50\text{cy/mm} \quad (3.12)$$

And diffraction limit resolution of the reflective spectrometer can be computed

From equation (3.1) as

$$\Delta x = \frac{1.22 \times (880 \times 10^{-9}\text{m}) \times 203 \times 10^{-3}\text{m}}{30 \times 10^{-3}\text{m}}, \quad (3.13)$$

$$\Delta x = 7.2 \mu\text{m}. \quad (3.14)$$

The sensor size of  $10\mu\text{m}$ , so the resolution is limited by the size of the sensor as follows  $\Delta x$  is equal to  $7.2\mu\text{m}$ , So the frequency maximum of the systems is  $\xi = 50 \text{ cy/mm}$ .

### 3.5 Verification of the maximum imaging depth in SD-OCT

To verify the performance of the spectrometer for SD- OCT, we used the spectrometer as a detector in our custom developed SD-OCT system that has the similar setup as illustrated in Figure 1.3 in chapter 1. When using the spectrometer as a detector in SD- OCT system, an effective spectral resolution of the implemented spectrometer can be verified through the measurement of the drop-off of the OCT signal amplitude at different depth positions. In this measurement, we acquired OCT depth scans at 27

different depth positions with  $100\ \mu\text{m}$  apart. The depth position was varied by fixing the sample reflector at the focal plane of the objective lens and moving only the reference mirror that was mounted on a precision translation stage, having a  $10\ \mu\text{m}$  resolution. The imaging depth of the SD-OCT system is typically determined by the 10 dB fall-off of the amplitude, i.e. a magnitude drop of about 10 times. Furthermore, the effective spectral resolution of the spectrometer can be estimated from the inverse Fourier transformation of the fall-off curve of the signal amplitude.



## CHAPTER IV

### RESULTS AND DISCUSSION

#### 4.1 MTF measurement

##### 4.1.1 Lenses based spectrometer

Figure 4.1 shows MTF curves, i.e. plots between modulation contrast of the spectral interference and modulation frequency in cycles/millimeter, of 3 different zones of the spectrometer's sensor. Each measured MTF curve represents spectral resolution performance of the spectrometer in each region of the line array sensor.

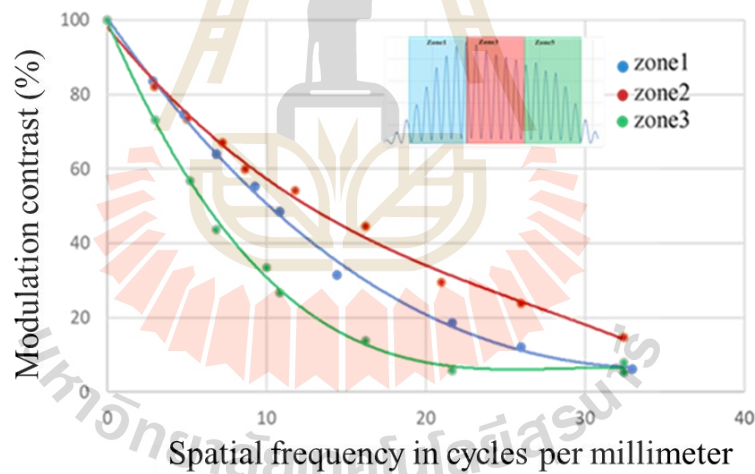


**Figure 4.1** MTF plots of different regions of the sensor obtained by the algorithm shown in Figure 3.3.

The result implies that the sensor is tilted as compared with the focal line, where the best focus is in zone 2 and the worst focus is in zone 5. To determine the tilt

direction, an additional experiment was conducted as to be discussed in the following section.

#### 4.1.2 Reflector based spectrometer

Figure 4.2 shows MTF curves of 5 different zones of the spectrometer's sensor. Each measured MTF curve represents the spectral resolution performance of the spectrometer in each region of the line array sensor. The MTF results reveal that the spectral resolution in zone 1, zone 2 and zone 3, i.e. of the sensor, was much better than that in zone 4 and zone 5.

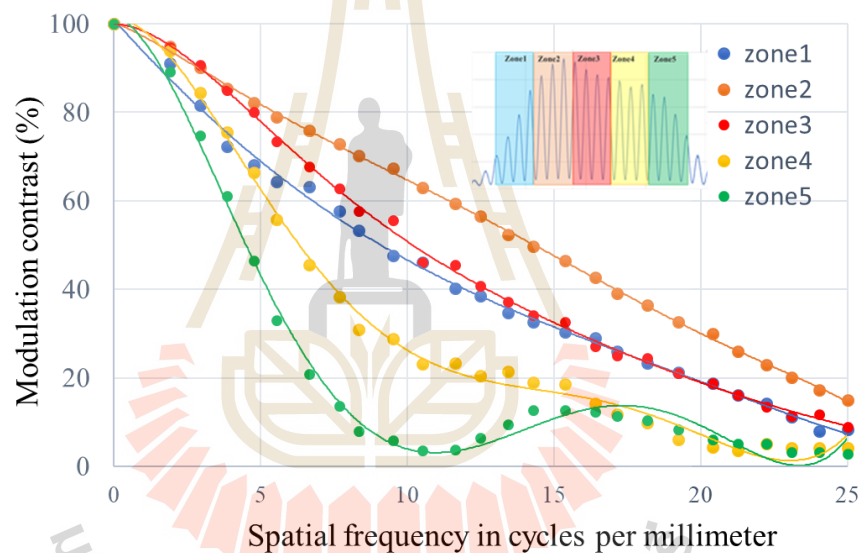


**Figure 4.2** MTF plots of different regions of the sensor obtained by the algorithm shown in Figure 3.3.

The result implies that the sensor is tilted as compared with the focal line, where the best focus is in zone 2 and the worst focus is in zone 5. To determine the tilt direction, an additional experiment was conducted as will be discussed next.



## 4.2 Measurement verification

We performed measurement verification by adjusting alignment of the system and the measuring MTF curves. To adjust the focus of the sensor we chose two adjustments that are the collimator of the incident beam on the grating and the vertical tilt of the off-axis Parabolic Mirror with  $45^\circ$ , the mirror before the sensor. Adjusting the collimator introduced defocus and adjusting the vertical tilt of the off-axis Parabolic Mirror with  $45^\circ$  cause vertical shift of the focus on the sensor. Figure 4.3 shows MTF curves when adjusting the collimator by +0.1 mm causing slight convergence of the collimation. The MTF curves reveals that adding convergence of the collimated beam led to significant improvement of the spectral resolution in zone 1 but degrade the resolution in the rest of the sensor region as compared with Figure 4.2.

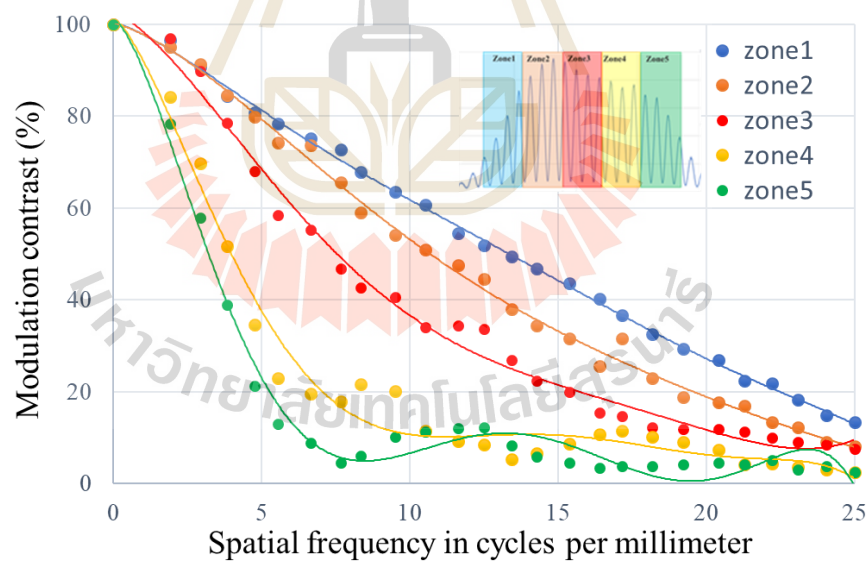


**Figure 4.3** MTF plots of different regions of the sensor after adding defocus of the collimator by +0.1 mm.

Figure 4.4 shows MTF curves when we adjust collimator by -0.1 mm causing slight divergence of the collimation. From Figure 4.4, -0.1 mm defocus of the collimated beam clearly shows resolution improvement in zone 4 and 5 with acceptable MTF drop in zone 1 as compared with Figure 4.2 and 4.3. Therefore, this is the correct direction of collimator adjustment to obtain optimum focus of the spectrometer. When comparing Figure 4.3 and Figure 4.4, the MTF curve of zone 4 and zone 5 when the collimator is adjusted by -0.1 mm appears to provide better results than when it is adjusted by +0.1 mm. The MTF curve drops because of the defocus at the sensor as shown in Figure 4.5.

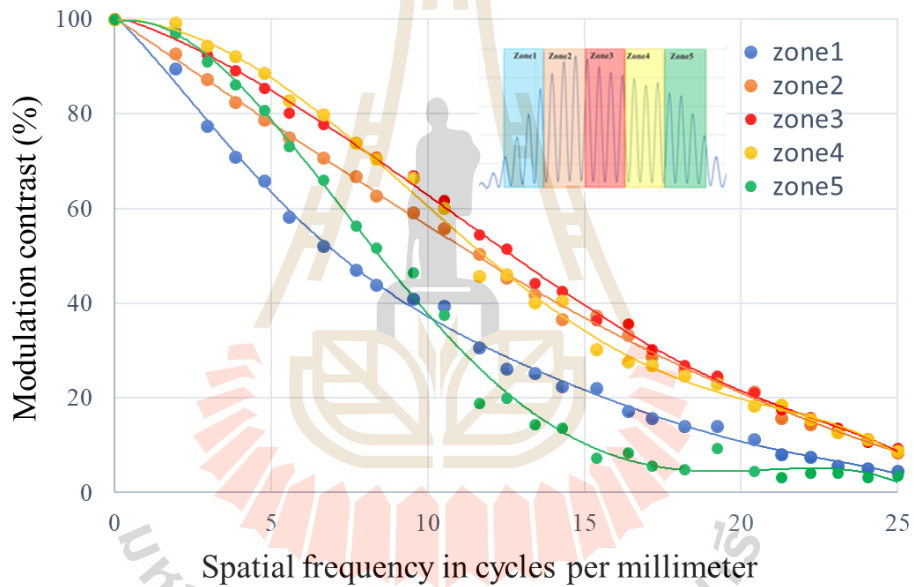


**Figure 4.4** MTF plots of different regions of the sensor after defocus of the collimator by -0.1 mm.

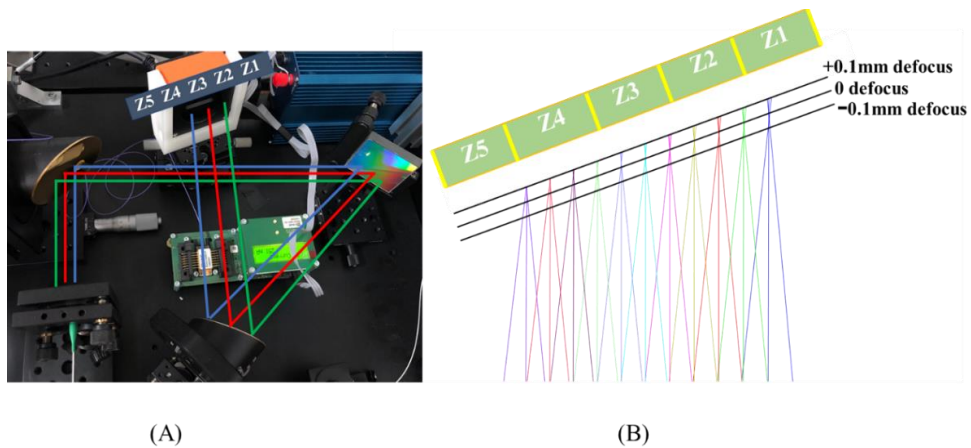


**Figure 4.5** (A) Regions of the sensor of the spectrometer. (B) sensor defocus as simulated in code V software.

In addition, tilting the mirror up and down cases the focal plane of the system to shift up and down respectively, as compared with the sensor. Figure 4.6 and Figure 4.7 show MTF curves when we adjust off-axis Parabolic Mirror with  $45^\circ$  up by 2 degrees and down 2 degrees, respectively.

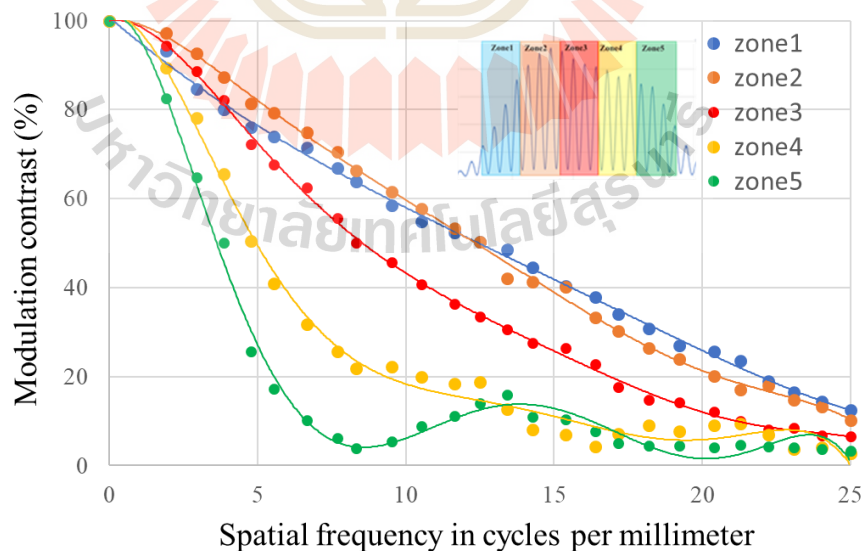


**Figure 4.6** MTF plots of different regions of the sensor after tilting up the off-axis Parabolic Mirror with  $45^\circ$  by 2 degrees.

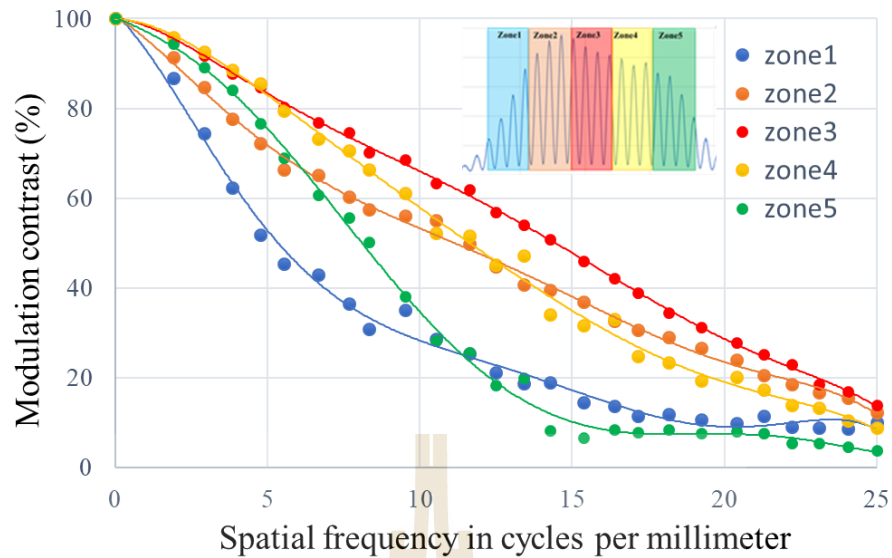


**Figure 4.7** MTF plots of different regions of the sensor after tilting down the off-axis Parabolic Mirror with  $45^\circ$  by 2 degrees.

In addition, the measurement results can be analyzed by zone. Figure 4.8 presents the comparison of MTF performance at difference defocus of the collimator in 5 different zones. The blue line represents the starting point, i.e. the line before defocus adjustments. The red line represents +0.1 mm defocus. The green line represents -0.1 mm defocus.

From Figure 4.8, we observe that the green lines in the figure (C), (D), and (E) shown better MTF performance as compared with that of other colour lines. The results show that -0.1 mm defocus of the collimator leads to resolution improvement at zone 3, 4, and 5 of the sensors. However, the resolution in zone 1 improved with +0.1 mm defocus of the collimator. The overall result implies that the line sensor is tilted as relative to the focal plane as illustrated in Figure 4.5.

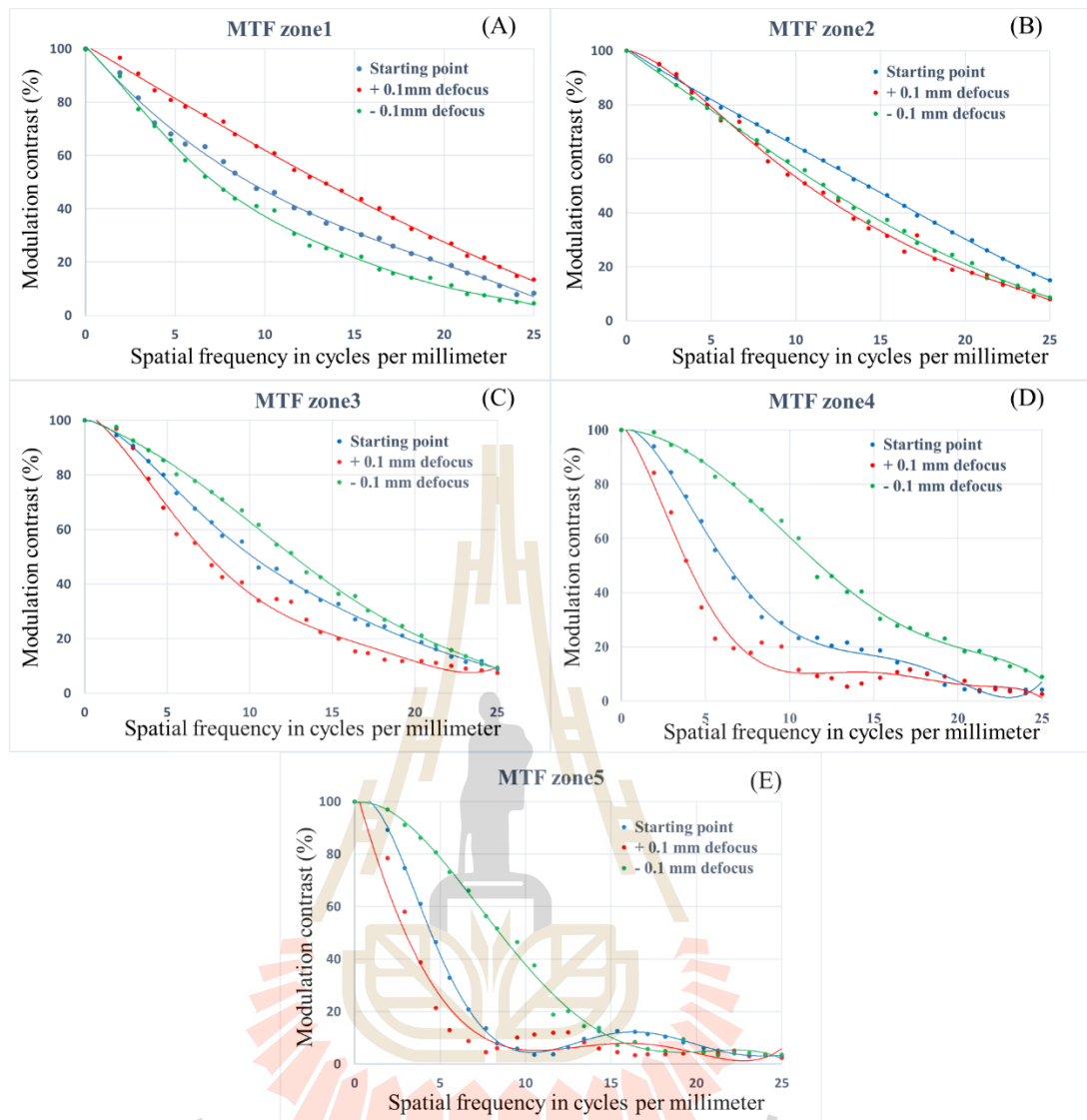


**Figure 4.8** Comparison of MTF performance at difference defocus of the collimator in (A) zone 1, (B) zone 2, (C) zone 3, (D) zone 4, and (E) zone 5.

### 4.3 SD-OCT verification

When we use the spectrometer as a detector in SD-OCT system, an effective spectral resolution of the implemented spectrometer can be characterized through the measurement of the amplitude drop as a function of depth positions. In our measurement, we measured the axial PSFs at 27 different depth positions with  $100 \mu\text{m}$

apart and extracted their peak amplitudes and positions. The depth position was altered by fixing the sample reflector at the focal plane of the objective lens and moving only the reference mirror that was mounted on a precision translation stage, having a  $10\ \mu\text{m}$  resolution. An example of a spectral interference fringe at arbitrary depth position is demonstrated in Figure 4.9(A-C). It is known that the finite spectral resolution will lead to the reduction of the fringe visibility (i.e., the modulation depth) as the fringe frequency increases. This effect appears as the amplitude dropping of an axial point spread function (PSF) over the depth after the Fourier transformation of the spectral fringe as illustrated in Figure 4.9(D-F). As a result, by tracing the shape of the amplitude drop-off over depth positions as shown in Figure 4.10(A), the effective spectral resolution of the spectrometer can be quantitatively determined.

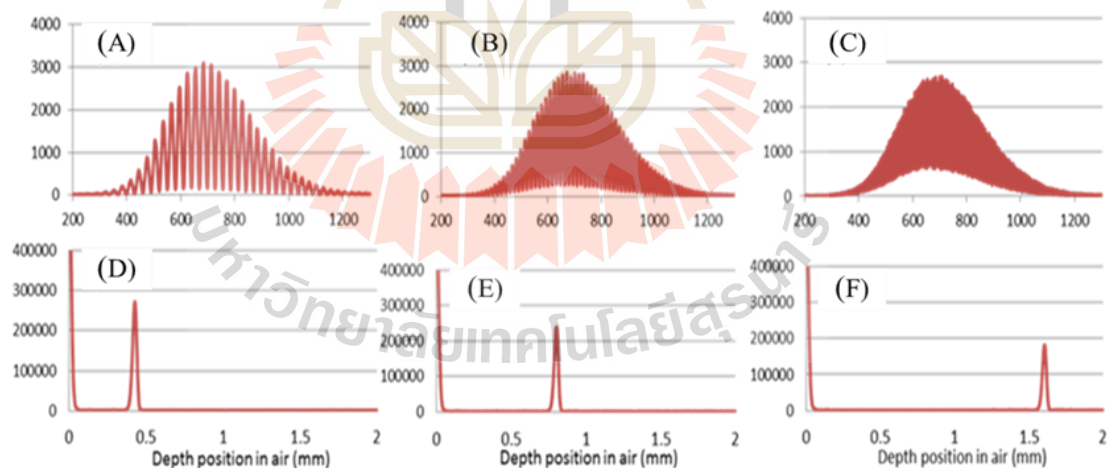


**Figure 4.9** (A-C) Examples of spectral interference signals as detected by the spectrometer and (D-F) its corresponding depth profiles obtained through the Fourier analysis.

### 4.3.1 Lenses based spectrometer

From Figure 4.10(A), the imaging depth of the SD-OCT system is typically determined by the 10 dB fall-off of the amplitude, i.e. a magnitude drop of about 10 times, which corresponds with about 2.5 mm for this system. Furthermore, using the information from the plot in Figure 4.10(A), the shape of the spectral resolution of the spectrometer can be obtained by inverse Fourier transform of the trace of the maximum amplitude of those measured axial PSFs. We first performed the polynomial curve-fitting on the extracted peaks data as indicated by a solid line in Figure 4.10(A) and then inverse Fourier transform the fitted curve to obtain the profile of the effective spectral resolution of the implemented spectrometer as shown in Figure 4.10(B). The spectral line width was then quantified by measuring the full-width at half-maximum (FWHM) of the spectral profile in Figure 4.10(B) to be about 0.18 nm.

As previously mentioned, the effective spectral resolution of the spectrometer ( $\delta\lambda$ ) is determined by either the pixel size of the sensor or an optical resolution of the focusing optics whichever larger as expressed by equation (2.23). For example, the required effective spectral resolution for the aimed 1.5 mm imaging depth in biological sample (e.g. using  $n \approx 1.4$ ) was computed to be about 0.09 nm for the 840 nm central wavelength. However, the full-width at half-maximum (FWHM) of the spectral profile in Figure 4.10(B) was measured to be about 0.18 nm, which was about twice larger than the targeted spectral resolution of 0.09 nm.

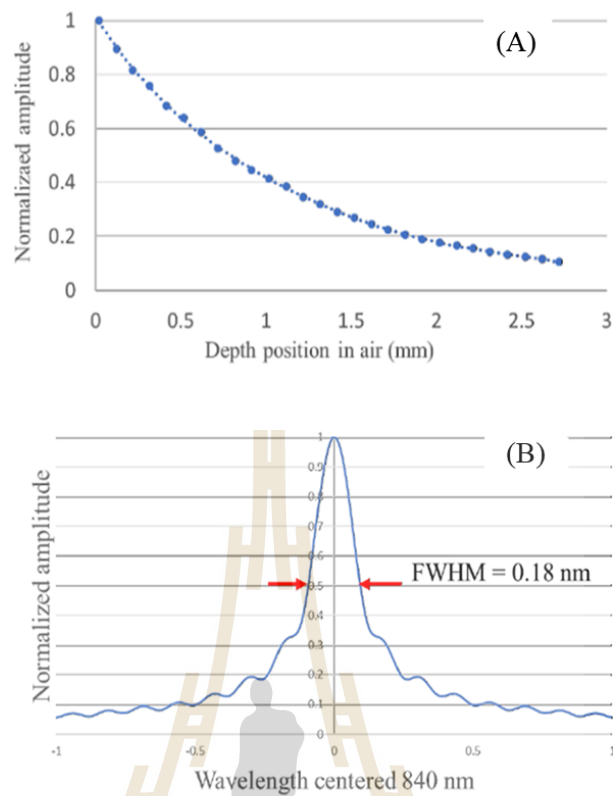


**Figure 4.10** (A) Plot of the peak amplitude of the SD-OCT signals measured at different depth positions in air. Figure 4.10 (B) Inverse Fourier transform of a fitted curve, representing the shape of the overall effective spectral resolution of the Lenses based Spectrometer.

#### 4.3.2 Reflector based spectrometer

From Figure 4.11(A), the imaging depth of the SD-OCT system was measured to be about 2.5 mm for this system. Furthermore, using the information from the plot in Figure 4.11(A), the shape of the spectral resolution of the spectrometer can be obtained by inverse Fourier transform of the trace of the maximum amplitude of those measured axial PSFs.



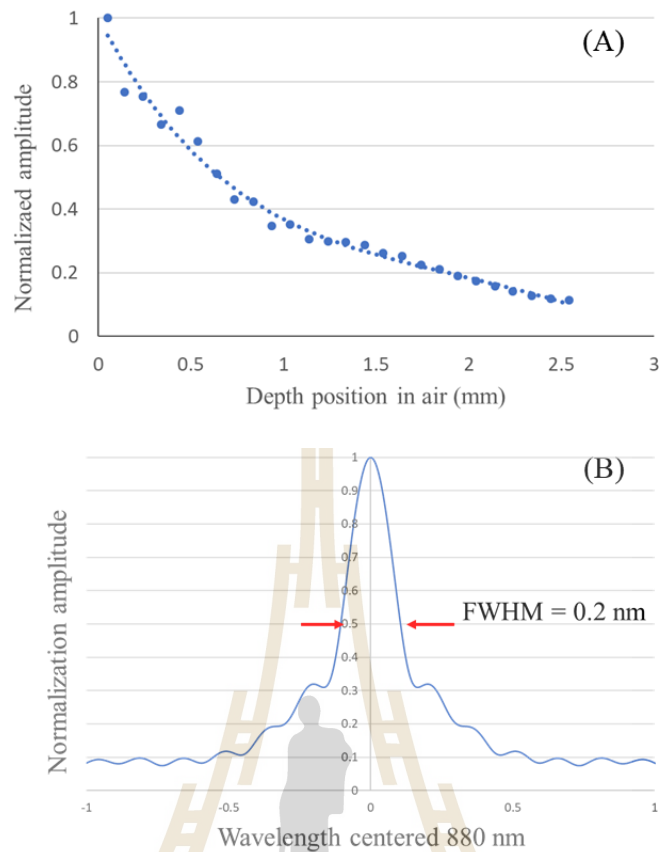


**Figure 4.11** (A) Plot of the peak amplitude of the SD-OCT signals measured at different depth positions in air. Figure 4.11 (B) Inverse Fourier transform of a fitted curve, representing the shape of the overall effective spectral resolution of the Reflective Spectrometer.

Inverse Fourier transform of the fitted curve in Figure 4.11(A) yields the profile of the effective spectral resolution of the implemented spectrometer as shown in Figure 4.11(B). The spectral linewidth was then quantified by measuring the FWHM of the spectral profile in Figure 4.11(B) to be about 0.2 nm which was about twice larger than the targeted spectral resolution of 0.09 nm.

#### 4.4 Comparison of the MTF measurement and the SD-OCT signal drop-off

To verify the relation between the MTF curves that were directly measured from the modulated spectra and the SD-OCT signal drop-off curve, we converted the modulation frequency (i.e. the x-axis) of the MTF plots in Figure 4.1 to the depth location in air. Figure 4.12 shows the comparison the MTF curves as measured in section 4.1 with the SD-OCT signal drop-off curve as measured in section 4.3. The result verifies that the SD-OCT signal drop-off curve is approximately an average of the MTF curves of all zones.

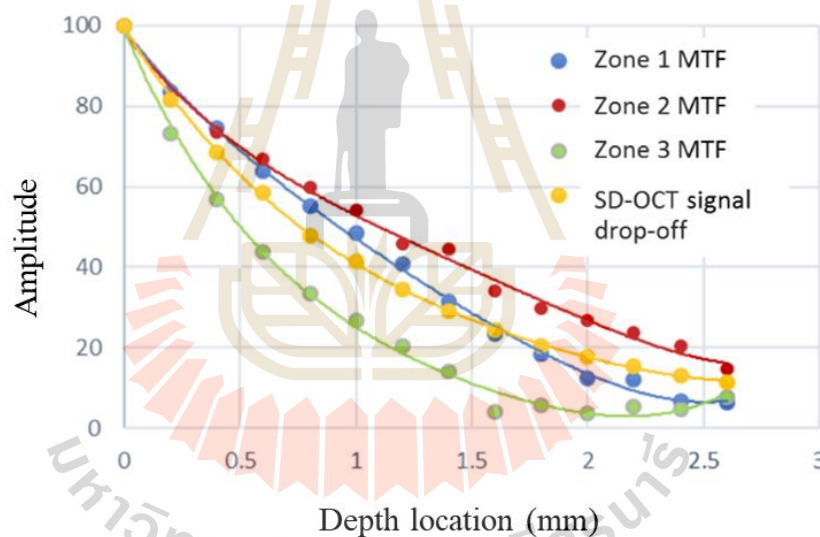


**Figure 4.12** Comparison of the MTF curves and the SD-OCT signal drop-off.

#### 4.5 Imaging performance of the system

We have verified the imaging performance of the developed SD-OCT system on various biological samples. Figure 4.13 shows an example of in vivo imaging of human skin using the implemented spectrometer-based SD-OCT system. The cross-sectional image of skin as captured by the developed system in Figure 4.13(B) clearly

shows the boundary between epidermis and dermis regions of the skin. In addition, some sweat ducts can be observed. Figure 4.13(C) shows the *en face* image of the dermis surface of the skin that was reconstructed from a 3D dataset acquired by the SD-OCT system. Further optimization of the effective spectral resolution of the spectrometer would allow for better visualization of tissues in the deep region of the dermis. The proposed algorithm in this paper will aid the alignment processes of the spectrometer unit to obtain the optimum spectral resolution of the overall system.

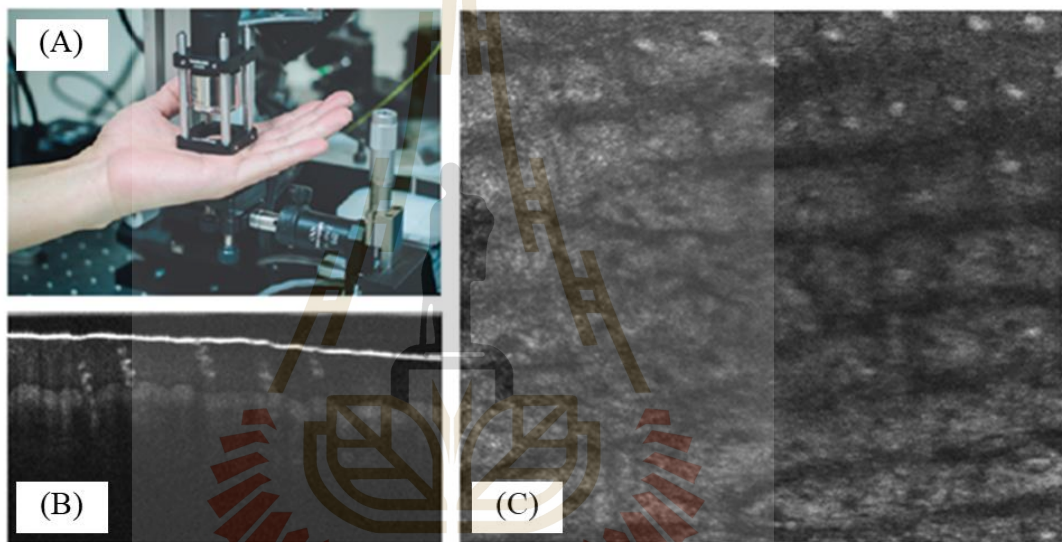


**Figure 4.13** An example of in vivo skin imaging obtained by the developed SD-OCT.

# CHAPTER V

## CONCLUSION

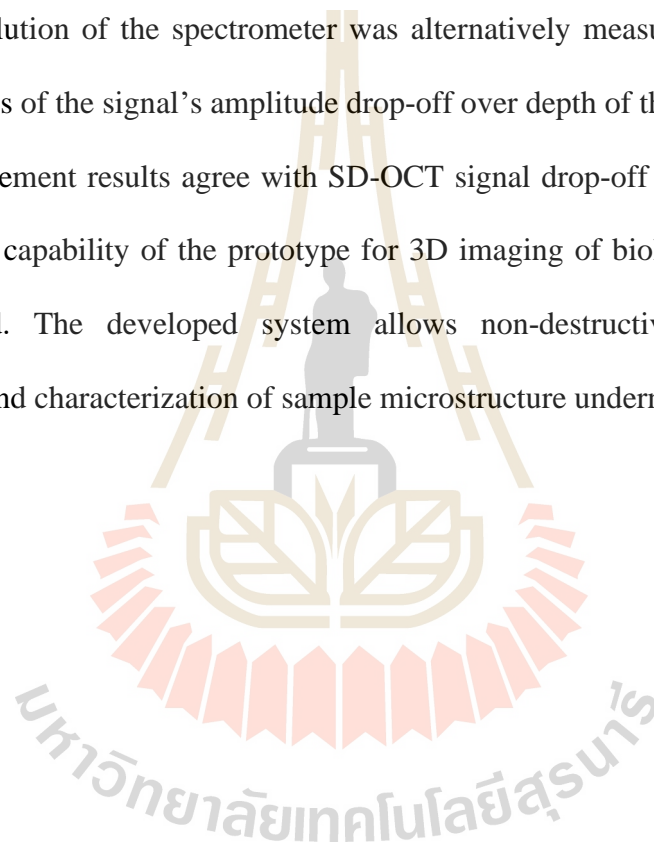
In SD-OCT, the depth of imaging of the system is highly related to the spectral resolution of a spectrometer that is used to detect spectral interference fringe. The higher the spectral resolution, the longer the imaging depth range. CCD and CMOS line array sensor are commonly used as a detector in a high-speed spectrometer for SD-OCT. The resolution of the spectrometer is either limited by the number and pixel size of a line array sensor or the optical resolution performance of the imaging optics before the sensor. Most of the time, the effective spectral resolution is limited by aberrations of imaging optics of the spectrometer. Therefore, the best alignment of the spectrometer is essential to minimizing the aberration of the spectrometer and hence maximizes imaging depth of the SD-OCT system.

In this work, we have developed a procedure to measure the MTF performance of a spectrometer during its alignment process. The proposed technique can quantify MTF curves, i.e. interference contrast versus spatial frequency, at different regions of the line-array sensor of the spectrometer, which has been proven to be useful information for optical alignment of the spectrometer and obtain its best spectral resolution performance.

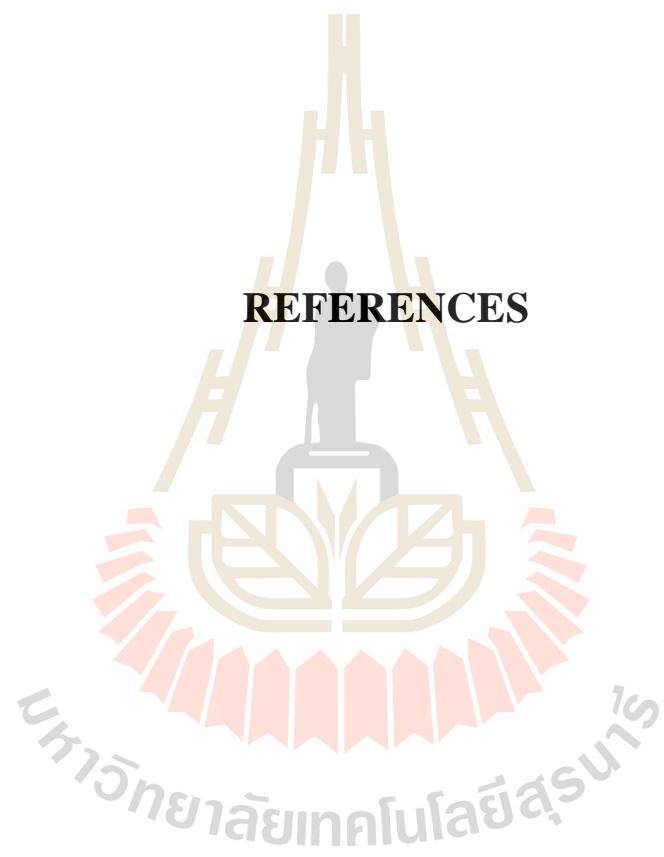
To experimentally verify the developed algorithm, two spectrometers, i.e. lenses-based and reflector-based spectrometers, that utilized only off-the-shelf optical components was designed and implemented. An example of MTF curves measured by

the proposed procedure was demonstrated. The ability to measure the MTF curves of different regions of the array sensor of the spectrometer during its alignment allowed for tracing the direction of misalignment between the focal line of the focusing optics and the line array sensors. This information has been proven to be useful for determining the direction of adjustment of the spectrometer alignment.

Furthermore, by using the implemented spectrometer in SD-OCT system, the spectral resolution of the spectrometer was alternatively measured by analyzing the characteristics of the signal's amplitude drop-off over depth of the overall system. The MTF measurement results agree with SD-OCT signal drop-off measurement data. In addition, the capability of the prototype for 3D imaging of biological microstructure was verified. The developed system allows non-destructive and non-invasive monitoring and characterization of sample microstructure underneath its surface.



## REFERENCES



## REFERENCES

- An, L., Li, P., Shen, T. T., and Wang, R. (2011). High speed spectral domain optical coherence tomography for retinal imaging at 500,000 A-lines per second. **Biomedical optics express**. 2(10): 2770-2783.
- Bashkansky, M., Duncan, M., Kahn, M., Lewis III, D., and Reintjes, J. (1997). Subsurface defect detection in ceramics by high-speed high-resolution optical coherent tomography. **Optics letters**. 22(1): 61-63.
- Born, M., Wolf, E., and Bhatia, A. (1999). Principles of Optics, seventh (expanded) ed. **Cambridge U. Press, Cambridge, UK.**
- Bouma, B., and Tearney, G. (2002). Handbook of Optical Coherence Tomography (Marcel Dekker, New York, 2002).
- Choma, M. A., Sarunic, M. V., Yang, C., and Izatt, J. A. (2003). Sensitivity advantage of swept source and Fourier domain optical coherence tomography. **Optics express**. 11(18): 2183-2189.
- Czerny, M., and Turner, A. (1930). On the astigmatism of mirror spectrometers. **Z. Phys.** 61(11-12): 792-797.
- De Boer, J. F., Cense, B., Park, B. H., Pierce, M. C., Tearney, G. J., and Bouma, B. E. (2003). Improved signal-to-noise ratio in spectral-domain compared with time-domain optical coherence tomography. **Optics letters**. 28(21): 2067-2069.
- Fan, C., Wang, Y., and Wang, R. K. (2007). Spectral domain polarization sensitive optical coherence tomography achieved by single camera detection. **Optics express**. 15(13): 7950-7961.

- Fercher, A. F., Hitzenberger, C. K., Kamp, G., and El-Zaiat, S. Y. (1995). Measurement of intraocular distances by backscattering spectral interferometry. **Optics Communications**. 117(1-2): 43-48.
- Fujimoto, J. G., Bouma, B., and Tearney, G. (2002). Handbook of optical coherence tomography. **Chapter 1, Edited by GR Bouma, GJ Tearney, Marcel Dekker Inc.**
- Geary, J. M. (2002). *Introduction to lens design: with practical ZEMAX examples*: Willmann-Bell Richmond.
- Götzinger, E., Pircher, M., and Hitzenberger, C. K. (2005). High speed spectral domain polarization sensitive optical coherence tomography of the human retina. **Optics express**. 13(25): 10217-10229.
- Grulkowski, I., Gora, M., Szkulmowski, M., Gorczynska, I., Szlag, D., Marcos, S., Kowalczyk, A., and Wojtkowski, M. (2009). Anterior segment imaging with Spectral OCT system using a high-speed CMOS camera. **Optics express**. 17(6): 4842-4858.
- Huang, D., Swanson, E. A., Lin, C. P., Schuman, J. S., Stinson, W. G., Chang, W., Hee, M. R., Flotte, T., Gregory, K., and Puliafito, C. A. (1991). Optical coherence tomography. **science**. 254(5035): 1178-1181.
- Lawman, S., Dong, Y., Williams, B. M., Romano, V., Kaye, S., Harding, S. P., Willoughby, C., Shen, Y.-C., and Zheng, Y. (2016). High resolution corneal and single pulse imaging with line field spectral domain optical coherence tomography. **Optics express**. 24(11): 12395-12405.
- Lee, S.-W., Jeong, H.-W., Ahn, Y.-C., Jung, W., Chen, Z., and Kim, B.-M. (2009). *Axial resolution and depth range of high-resolution spectral domain optical*



*coherence tomography at 1.3  $\mu\text{m}$* . Paper presented at the Optical Coherence Tomography and Coherence Domain Optical Methods in Biomedicine XIII.

Leitgeb, R., Hitzenberger, C., and Fercher, A. F. (2003). Performance of fourier domain vs. time domain optical coherence tomography. **Optics express**. 11(8): 889-894.

Meemon, P., Palawong, K., and Pongchalee, P. (2014). *Simplified methods of design, implementation, and characterization of a spectrometer-based FD-OCT*. Paper presented at the Three-Dimensional and Multidimensional Microscopy: Image Acquisition and Processing XXI.

Ohlmann, R., and Mego, A. (1966). Alignment of Fastie-Ebert Spectrometers Using He-Ne Laser. **Review of Scientific Instruments**. 37(4): 530-531.

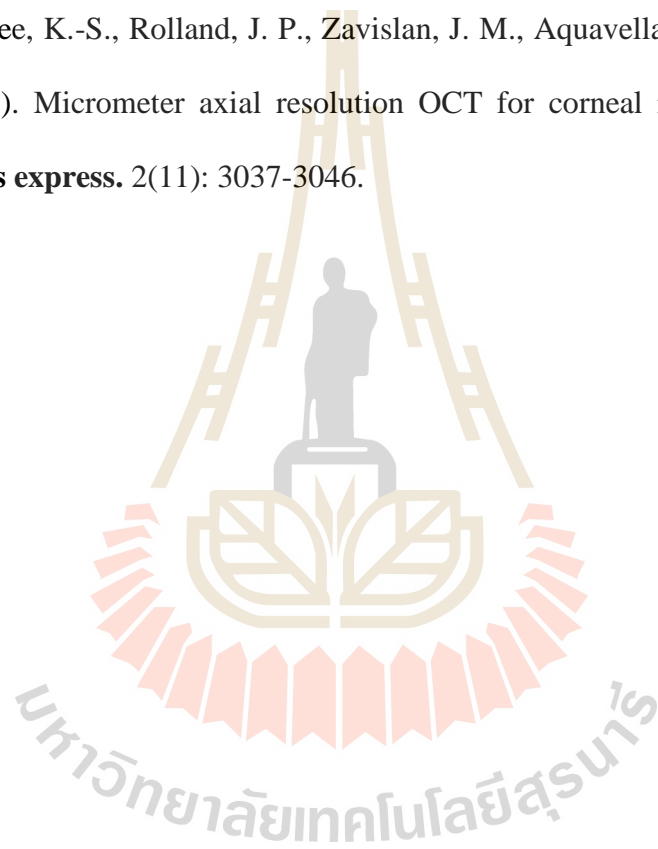
Potsaid, B., Gorczynska, I., Srinivasan, V., Chen, Y., Jiang, J., Cable, A., and Fujimoto, J. G. (2008). Ultrahigh speed spectral/Fourier domain OCT ophthalmic imaging at 70,000 to 312,500 axial scans per second. **Optics express**. 16(19): 15149-15169.

Wang, L., and Wu, H.-i. (2007). *Biomedical optics: Principles and imaging* wiley. **New York**.

Wojtkowski, M., Leitgeb, R., Kowalczyk, A., Bajraszewski, T., and Fercher, A. F. (2002). In vivo human retinal imaging by Fourier domain optical coherence tomography. **Journal of biomedical optics**. 7(3): 457-464.

Woolliams, P., Ferguson, R. A., Hart, C., Grimwood, A., and Tomlins, P. H. (2010). Spatially deconvolved optical coherence tomography. **Applied optics**. 49(11): 2014-2021.

- Woolliams, P., and Tomlins, P. (2011). The modulation transfer function of an optical coherence tomography imaging system in turbid media. **Physics in Medicine & Biology**. 56(9): 2855.
- Xi, P., Mei, K., Bräuler, T., Zhou, C., and Ren, Q. (2011). Evaluation of spectrometric parameters in spectral-domain optical coherence tomography. **Applied optics**. 50(3): 366-372.
- Yadav, R., Lee, K.-S., Rolland, J. P., Zavislan, J. M., Aquavella, J. V., and Yoon, G. (2011). Micrometer axial resolution OCT for corneal imaging. **Biomedical optics express**. 2(11): 3037-3046.



## CURRICULUM VITAE

**Name** Miss Jiraporn Saenjae

**Date of Birth** 14 March 1991

**Place of Birth** Phrae, Thailand

### Education

- 6 March 2014, Bachelor Degree of Science in Physics (First Class Honors), UNIVERSITY OF PHAYAO.

### Publications

- Saenjae, J., Saetiew, J., Palawong, K., and Meemon, P. (2017). An experimental procedure for quantitative evaluation of spectral resolution of spectrometer-based spectral domain optical coherence tomography. In 2017 10th Biomedical Engineering International Conference (BMEiCON) (pp. 1-5). IEEE.

### Awards

- Panomsak Meemon, Kunakorn Palawong, Racha Pongchalee, Jadsada Saetiew, Jiraporn Saenjae. High-speed infrared microscope for nondestructive 3D cross-sectional imaging of biological samples. Excellent Award, Innovation and Technology Exposition (IPITEx 2015).
- Panomsak Meemon, Jadsada Saetiew, Jiraporn Saenjae. Infrared Microscope for non-contact thin film thickness topography. Good Award, Innovation and Technology Exposition (IPITEx 2018).